TITLE A STUDY OF SHALLOW IMPLANTS IN SILICON BY SECONDARY ION MASS SPECTROMETRY

AUTHOR Harvey Stuart Fox

INSTITUTION and DATE University of Warwick 1989

A STUDY OF SHALLOW IMPLANTS IN SILICON BY SECONDARY ION MASS SPECTROMETRY

by

Harvey Stuart Fox BSc(Hons).

A Thesis for the Degree of
Doctor of Philosophy
of the
University of Warwick

Physics Department

March 1989

CONTENTS

LIST OF FIGURES

LIST OF TABLES

ACKNOWLEDGEMENTS

I would like to acknowledege the help of the following people during the course of the project and during the preparation of this thesis.

Firstly, I would like to thank Professor E.H.C.Parker for his supervision and to the SERC and GEC Research who funded the project under a case award.

I would particularly like to thank Dr. M.G.Dowsett for his helpful advice and knowledge without which this thesis would not be possible. Thanks also to Dr. D.Godfrey of GEC Hirst Research centre, my industrial supervisor, for the preparation of the implants used in chapter 4 and to Mr. R.F. Houghton for the growth of the silicon caps. Also Dr. D.S. McPhail for teaching me how to use EVA 2000 and the after hours discussions that made the period of this project seem to fly by.

To all the members of the ASR Group at the University of Warwick and the City of London Polytechnic together with the technical staff, Mr. P. Driscoll, Mr. J. Heal, Mr. T. Naylor, Mr. R. Bull and Mr. B.Sheffield, I thank you all for your help and advice over the past few years.

Finally I would like to thank my parents for their support over my student career and their patience during the preparation of this thesis.

DECLARATION

This thesis is submitted to the University of Warwick in support of my application to the degree of Doctor of Philosophy. It contains an account of my work in the Department of Physics at The City of London Polytechninc and the department of Physics at the University of Warwick during the period October 1984 to September 1988 under the supervision of Professor E.H.C.Parker. No part of this thesis has been used previously in a degree thesis submitted to this or any other University. The work described is the result of my own research except where specifically acknowledged in the text.

March 1989 Harvey S. Fox

SUMMARY

This project investigates the analysis of shallow implants by secondary ion mass spectrometry (SIMS) and the problems that arise from it.

Ion implantation is now almost exclusively used in the manufacture of modern very large scale integration devices. The quantification of these implants can be carried out very successfully by SIMS. However the distortions that are present in any SIMS analysis are emphasised when the implanted layer is less than 100nm below the surface.

In order to characterize these distortions, it is necessary to be able to accurately parameterize the implant profile. Taking moments of the data was found to be a reliable method of doing this without constructing a distribution.

Once a parameterizing method was found the differential shift was investigated in silicon, with and without a Si-MBE grown capping layer. The results suggested that the differential shift may be a depth dependant phenomenon.

The effect of the amorphization of a crystal on ion implantation was investigated with respect to the change in sputter rate going through the damaged region. The effect of uneven etching on this study is discussed in detail.

In order to overcome this uneven etching two different raster scan units are discussed. One, is a new totally computer controlled device for use on a new SIMS instrument. The other is a modification to an existing scan unit. This second unit has been used to make craters that are flat to 0.05%

CHAPTER 1

DEPTH PROFILING

1.0 Overview

This chapter contains an overview of the thesis as a whole and then introduces SIMS depth profiling. It considers the sputtering process and secondary ion emission as well as the causes of profile distortions arising from the bombardment process. Other causes of profile broadening are also discussed. The altered layer produced in the sample under ion bombardment is looked at in detail.

1.1 Thesis Introduction

One of the main techniques used in the production of integrated circuits is ion implantation. It is important to SIMS also, as a source of reference standards. In order to quantify depth profiles properly, it is necessary to be able to model an implant accurately. One method of doing this is to determine the first four moments of the implant profile and this is discussed in chapter three.

Once a method of characterizing implants has been decided on, it is then possible to use these techniques to measure how a feature of an implant (e.g. the projected range) changes under different analysis conditions. One distortion that arises from the

formation of the altered layer is the so called differential shift. This occurs when primary ions of different energies are used to bombard the sample and then no account is taken during post analysis processing of the different pre-equilibrium dose required to form the altered layer. In chapter four the differential shift is investigated in three technologically important matrices containing shallow implants. The effect of the altered layer on the measurement of the projected range is discussed and a method of overcoming this by growing a capping layer on the sample is described.

The depth scale of a SIMS depth profile is calibrated after the analysis and usually a constant sputter rate is assumed to have pertained throughout the analysis. The presence of highly defected regions in the vicinity of the peak of an unannealed implant could affect the sputter rate and make the depth calibration less accurate. In chapter five this problem is addressed when an attempt to measure the effect in silicon by comparing the sputter rates in implanted samples containing different doses of boron is described. This leads to a discussion of the importance of flat bottomed craters to the success of a depth profile, since a non-uniform current density across a crater makes the drawing of reliable conclusions very difficult.

In chapter six the operation of two raster scan generators is discussed, one a redesign of a commercially

available unit, and the other a completely new design. The effect of the redesigned unit on the crater profiles is also discussed. Finally there is a chapter on the conlusions drawn from this study together with suggestions for further work.

1.2 Interaction of Primary Ions with Solids.

1.2.1 Collision Cascade

An energetic particle that bombards a solid at normal or near normal incidence, will, in general, be implanted some distance below the surface, at a depth that depends on the energy and mass of the primary particle and also on the composition of the target.

The primary particle slows down by interacting with target atoms by nuclear and electronic stopping processes (Sigmund 1969). A target atom that receives enough energy by nuclear stopping will be relocated away from its original position. In a crystalline material this means that it will be removed from a lattice site, thus generating a defect. This moving atom will, in turn, slow down by colliding with its neighbours and thus will produce secondary and tertiary particles moving in the solid. This mechanism occurs along the whole track of the primary particle and the total phenomenon is called the collision cascade and is shown in figure 1.1. The process takes $\approx 10^{-12}$s to die out (Sigmund 1974).

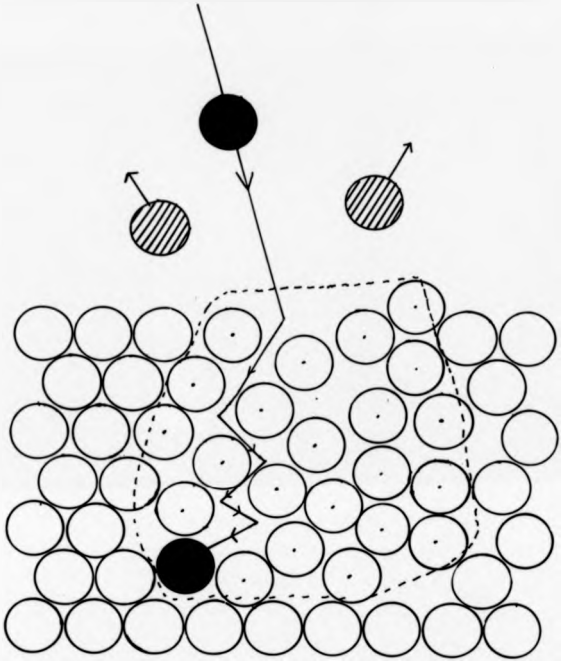

FIGURE 1.1. Schematic diagram of the collision cascade. The primary ion at the beginning and end of its track is shown in black. Relocated atoms are dotted. Sputtered atoms are shaded. The broken line shows the extent of the collision cascade within the material. The solid line shows the track taken by the primary ion.

The target itself will become diluted as a result of the build up of the primary species and thus at some later time, the sample composition will be different, both from the bulk and also from the original distribution of elements in the material.

If an atom in the collision cascade acquires enough energy to overcome the surface potential barrier and it is moving in the right direction, then that atom will be sputtered into the vacuum.

Approximately one sputtered atom in a thousand is ionised and this can be detected by a mass spectrometer as a secondary ion. The energy spectrum of the secondary ions, figure 1.2, exhibits a peak at ≈10eV, with a tail extending to higher energies. This means that most of the secondary ions are emitted from the top few monolayers of the target.

The full width at half maximum (FWHM) of the energy distribution contains information on the nature of the emitted ion. If the energy distribution is wide then the ion species is monatomic. However, the more atoms that are present in the ion, the narrower the distribution becomes. This fact can be exploited in removing some molecular interferences such as ^{75}As with $^{29}Si^{30}Si^{16}O$ (Chapter 4). This is achieved by applying a bias to the sample so that only ions with higher energies are transmitted through the energy bandpass of the instrument, and if a large enough bias is applied the

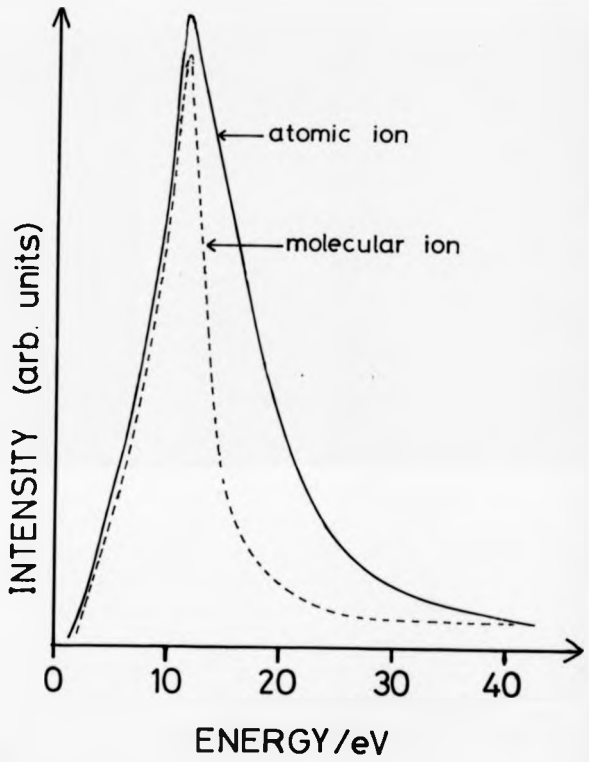

FIGURE 1.2. Energy spectrum showing the difference between atomic and molecular ions. Note, atomic ions have a high energy tail.

contribution of the cluster species can be negligible (Wittmaack 1976).

1.2.2 Atomic Mixing

As mentioned above, target atoms that are set in motion by collisions with the primary ion in the collision cascade will be relocated. This relocation gives rise to a phenomenon known as atomic mixing. This mixing is of two types: recoil mixing and random mixing.

If a primary ion collides with a target atom with a small impact parameter then it will be relocated in a direction along the track of the primary. This is recoil mixing. Random or isotropic mixing causes a general redistribution of material in the target.

These two processes, when taken together, cause a distortion to the final depth profile as follows:

Consider a layer of impurity atoms below the surface of a solid, figure 1.3a. As sputtering begins, the atoms in this layer are randomly redistributed causing the layer to broaden, figure 1.3b. This broadening increases as sputtering continues. When the instantaneous surface reaches the edge of the broadened layer, 1.3c, the first impurity atoms are sputtered and detected. Mixing continues all the time but those atoms that are sputtered are unavailable for relocation. This whole process results in the depth profile shown in figure 1.3d, this exhibits a steep leading edge and a long trailing edge.

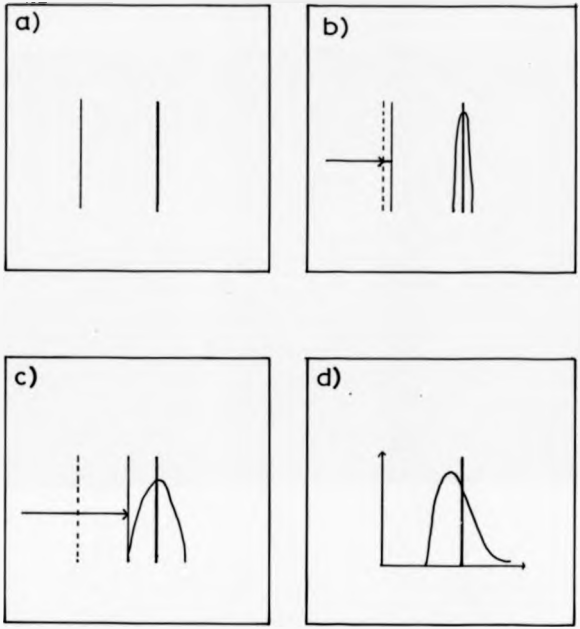

FIGURE 1.3. Schematic of profile broadening caused by atomic mixing. a) A layer of impurity is buried under the surface of a sample. b) Bombardment starts and the impurity begins to mixed symmetrically. c) The instantaneous surface meets the broadened region of impurity and the first impurity atoms are sputtered. d) The resulting depth profile showing how the SIMS signal responds to the processes shown in a-c. The profile has a characteristic sharp leading edge and a long trailing edge. The peak is also displaced from its initial position.

The decay length of the trailing edge is a good indication of the amount of mixing that has taken place (Vandervorst et. al. 1984), (Wittmaack 1984). Also, the peak of the profile does not coincide with the position of the original layer.

1.2.3 Altered layer

During ion bombardment, primary particles are accumulated into the material some distance below the surface. This has several effects:

1) The dilution of target material in the vicinity of the range of the implanted ions.

2) A relaxation current of material towards the surface. This occurs because the target cannot become superdense and therefore the target relaxes. This relaxation current is known as the Kirkendall effect (Collins 1986).

3) The build up of primary atoms occurs over a period of time and eventually a steady state condition is reached, where as many primary atoms are being sputtered as are being incorporated in the material (Williams 1979).

Before the steady state condition is reached, the changing amount of the primary species in the material also affects the final depth profile.

The sputter rate in this pre-equilibrium region is often different to that at steady state, and this leads

to an effect called the differential shift (Wach et.al. 1981). This is due to to the assumption of a constant sputter rate during the whole analysis period and has the effect of making a subsurface feature appear to move relative to the surface if the analysis is repeated at several energies.

The thickness of the pre-equilibrium region depends on the energy and bombardment angle of the primary species. At higher energies, the primary ions are implanted deeper into the material and therefore it takes longer for the steady state regime to occur.

For a given energy, changing the angle of incidence away from the normal, reduces the width of the pre-equilibrium region since less of the ion's momentum is directed inwards.

Some primary species e.g. argon, can diffuse through the target and accumulate at defect sites. Other species e.g. oxygen and caesium may react with the target atoms causing segregation effects to occur.

1.2.4 Segregation

Oxygen bombardment of silicon at normal incidence causes the formation of a buried silicon dioxide layer (Reuter et.al. 1980), (Hensel et.al. 1985), the presence of which can cause segregation effects to occur. This segregation has been observed for copper (Boudewijn

et.al. 1984), silver (Wittmaack et.al. 1987) and arsenic (Vandervorst et.al. 1986).

Silver segregation was observed by the study of a thin surface layer which was bombarded by oxygen. The SIMS crater produced was analysed by Rutherford Back Scattering spectrometry (RBS) and showed that after analysis ≈38% of the initial concentration of silver remained at the bottom of the crater. This leads to the conclusion that that the silver migrated in front of the advancing oxide.

For arsenic, the segregation was observed by exposing a low energy implant (5keV) at two different ion energies in a reactive ion etcher (RIE) and by SIMS. The decay lengths of the profiles produced were compared. For low energy SIMS analysis the decay length was 6.5nm. the high energy SIMS gave a decay length of 16nm.

The results from the ion etching were substantially different. The high energy decay length was 58nm and the low energy 17nm. These variations may be due to different experimental parameters between RIE and SIMS, but they both show that arsenic segregates in silicon.

There are segregation effects present in SIMS in most circumstances (Kirschner 1985). However, these usually manifest themselves as surface segregation which in turn leads to preferential sputtering (Kelly 1985). The effects considered here are different in that the segregation occurs away from the surface.

The data presented in the paper on silver segregation cited above indicates that segregation occurs in the pre-equilibrium period before an oxide layer has built up. Much work remains to be done in this area, particularly with respect to the arsenic/silicon system.

1.2.5 Emission of Secondary ions

The majority of the particles produced by sputtering will be neutral atoms, but a small proportion ($\approx 10^{-2}$ - 10^{-3}) will be ionised. The number of secondary ions emitted per incident primary atom is the ion yield (Williams 1979).

The ion yield is strongly dependant on the chemical environment of the sputtered particles. Thus the ion yield for some elements can vary by a factor of 10^3 depending on the matrix in which it is present.

In addition, ion yields can be enhanced by making the sputtering process occur in the presence of highly reactive elements. This can be achieved by either, using the reactive element as the primary ion, or by exposing the sample to an ambient of the reactive species, this is called flooding. Saturating the surface of a sample in this manner can increase the ion yield for many elements by a factor of 10^3 (Maul et.al. 1974).

Positive ion emission is enhanced by using an electronegative species such as oxygen. To enhance the negative ion yield electropositive caesium is used

(Wittmaack 1981). However, the use of these elements can raise some problems. Oxygen bombardment causes oxide formation below the sample surface and this can lead to segregation as mentioned above. Caesiation effects are also possible such as spot formation in GaAs (Miethe et.al 1985). The effect of implanting a large atom such as caesium into a lattice could also have a perturbing effect.

1.3 Other Causes of Profile Distortions

All the effects described above are fundamental to any ion bombardment technique. Profile distortions can also be caused by instrumental effects that can completely overwhelm the fundamental effects.

When a sample is sputtered, target atoms can be deposited on the adjacent parts of the vacuum system. This leads to a substantial build up of material on apertures, lenses and the walls of the system. When a subsequent sample is analysed, the deposited material can be resputtered leading to artificially high background levels of the deposited material (Deline 1983),(Wittmaack 1985). For example, analysing GaAs for silicon impurities after looking for dopants in a silicon matrix will show this effect. This continues until enough of the new sample has been sputtered to bury the previously deposited material. The time taken to do this is

dependant on the distance of the contaminated electrodes from the sample.

This memory effect can be diminished by ensuring that the surfaces that are deposited on are as far away as possible and hence the amount of deposited material per unit area is reduced. However, in instruments with a high extraction field this is not possible. A solution for these instruments is to use a dedicated extraction plate for each matrix to be investigated (Clegg 1986), (Huber et.al. 1986). This ensures that the resputtered material is the same as that being sputtered from the sample. These plates can be changed in-situ, thus avoiding breaking the vacuum in the sample chamber. This method of reducing memory effects is now incorporated into commercial magnetic sector instruments.

If there is any non-uniformity in the current density across the sputtered area uneven etching can occur causing a measurable uneveness in the crater bottom (see chapter 6) (McPhail et.al 1986a). The uneveness in the crater bottom produces a broadening in abrupt features in the sample and this effect scales with depth unlike the mixing effects described above.

Another instrumental effect is sample charging. If an insulating sample is profiled using an ion beam then charge build up at the surface occurs. This has the effect of shifting the energy spectrum of the sputtered ions, and, in an instrument with a low extraction field

the energy spectrum could be shifted completely out of the energy window (McPhail et. al. 1986b). In high extraction field instruments the amount of charging would have to be very great to have the same effect. However, if a high mass resolution or narrow energy window were being used, then a similar effect would be observed.

To compensate for sample charging an electron flood gun is often used to allow the charge build up on the sample surface to be neutralized (Wittmaack 1975). The amount of compensation is critical however, and in practice it can be very difficult to accurately compensate a sample over the whole profile. Another method to minimise charging is to use a primary atom beam which does not inject positive charge into the sample.

Coating the sample with gold before analysis and then sputtering through this can minimise charging in insulating samples. (McPhail et.al. 1986b). If the charging occurs because of the reverse biasing of p-n junctions in silicon for example, the target bias can be altered in response to detected changes in the secondary ion signal of a matrix species (Dowsett et.al. 1986c)

There are also sample specific effects that give rise to profile distortions. The presence of particulates on or near the surface within the gated area leads to spurious signals which affect the final depth profile. Using ion beam imaging (McPhail et. al. 1986b)

or post analysis gating (Chapter 2) can identify and remove these problems.

Defects within the material can give rise to non-uniform erosion due to changes in sample density over the beam scan. This leads to a incorrect calibration of the depth scale since the variations caused by the defects are not allowed for. Defects can also lead to changes in surface topography as described above. If the initial sample surface is not smooth, then this can also lead to beam induced roughening.

If a sample consists of two or more elements then preferential sputtering can occur (Kelly 1985). If the sputter yield of two elements from a matrix are different, then in the initial phase of a depth profile the species with the higher sputter yield will be depleted from the sample. The detected signal will indicate that there is more of this species than the one with a low sputter yield. After a period of time the sample will become so depleted of the first species that the signal will fall off and then reach a steady state value which is indicative of the concentration of that species in the bulk.

Post analysis effects are caused by variations in the sample going unnoticed and hence not being taken into account when calibration takes place. This is particularly apparent when profiling multilayer structures. The sputter rate, sputter yield and

ionization yield differs for each matrix, and if a constant sputter rate is assumed then the depth scale of the final profile will be incorrect. Sputter rates and yields have to be measured independently on standards of one matrix only, and then these factors used for the calibration of the sample under investigation. Systems such as TiSi/Si (Barlow et. al. 1988) and SiO_2/Si/Sapphire (Dowsett et. al. 1983a) are examples of how to correct for these variations. It is this effect of sputter yield variation that leads to the differential shift described in chapter 4. However, even allowing for these effects will not necessarily compensate for the variation in these parameters across the interface itself.

1.4 Conclusion

The interaction between the ion beam and a solid is a very complicated process, leading to the distortion of the original distribution of material in the sample. In order to obtain an accurate depth profile a great deal of care must be taken during analysis. Hence, the experimental conditions chosen for a depth profile should be such that those effects that produce the greatest distortion on the type of sample being examined are minimised. For example, when looking at a periodic doping structure, it is important that the atomic mixing

effects are minimised so as not to smear out rapid doping transitions.

Some of the effects mentioned in this chapter, such as the differential shift, can be corrected for during post analysis data processing, whilst others, such as atomic mixing cannot. However current research (e.g. Armour et.al 1988) is attempting to remedy this.

CHAPTER 2

INSTRUMENTATION

2.1 Introduction

SIMS depth profiling instruments are generally of two types: The ion microscope, e.g. Cameca IMS 4F (Thompson CSF) and the ion microprobe, e.g. EVA 2000. The ion microscope uses a mass spectrometer that produces a mass filtered stigmatic image of the analysed area. This can be observed on a screen or a discrete mapping device such as a resistive anode encoder to derive two dimensional information about the distribution of species of interest in the sample.

The ion microprobe does not produce a direct image and the detected signal consists of an analogue current measurement or the counting of discrete pulses.

These two modes of operation are not exclusive and an instrument with a double focussing mass spectrometer which produces an image can direct the ions leaving the mass spectrometer onto an ion detector to produce a count rate. Similarly, in microprobe mode an image can be formed by scanning the ion beam and synchronously scanning the X and Y plates of an oscilloscope with the intensity level being driven by a signal proportional to the detected ion signal.

In the course of this project the instrument used was EVA 2000, a computer controlled UHV quadrupole SIMS

instrument, operating as a microprobe, designed and built in house by Dowsett (Dowsett et.al. 1982a). A schematic diagram of EVA 2000 is shown in figure 2.1.

2.2 EVA 2000

To perform a high resolution SIMS depth profile the primary ion beam has to be monenergetic, contain only one ionised species, be free from ion or neutral contamination and be focussed into a small spot with a high current density. In EVA 2000 these conditions are obtained in the primary ion column

2.2.1 Primary Ion Column

The ion sources used on EVA 2000 are a Neilsen type cold cathode discharge which produces oxygen ions and a hot cathode discharge which produces argon ions.

The cold cathode discharge consists of a nickel cathode block with an aluminium cathode plate and aluminium cathode tip. The whole structure is cylindrically symmetric with the anode being an aluminium cylinder. The anticathode through which the ions emerge is a 0.5mm thick aluminium plate with a 0.5mm diameter hole in it (Dowsett et.al. 1983a). The whole discharge system is placed in a magnetic field of the order of 0.03T so that electrons travel in a helical path so as to increase the likelihood of a collision with a gas molecule before the plasma has been established. The

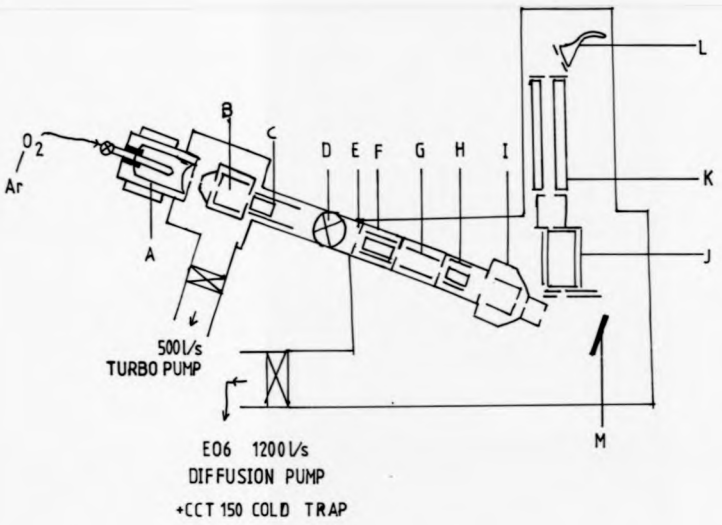

FIGURE 2.1. Schematic diagram of EVA 2000. Key: A) Cold cathode discharge. B) First lens. C) Wien Filter. D) Beam line valve. E) Pressure step. F) Quadrupole deflection plates. G) Two degree bend deflection plates. H) Quadrupole raster plates. I) Final Einzel Lens. J) Energy filter. K) Quadrupole mass spectrometer. L) Channeltron. M) Sample.

pressure in the discharge volume is maintained at $\approx 10^{-3}$ torr by use of a leak valve to introduce the gas.

Electrons leave the cathode and anticathode and travel towards the anode with the trajectory described above. Ionising collisions take place with the gas molecules producing positive ions. These are accelerated towards the cathodes and secondary electrons are emitted on impact. The effect of this is to produce a plasma which is contained within the anode volume. The oxygen ions leaving the source are mainly O_2^+ (>85%). The anode potential is ≈500V above the cathode potential for a cold cathode discharge. The discharge current is controlled in this mode and there is no direct control over the anode potential. The ions are self extracting since the plasma potential is ≈50V less than the anode potential so the ions leave the source with an energy of ≈450eV.

To accelerate the ions to the required energy there is an extraction gap of 1.5mm just after the the source and the accelerating potential is applied across this gap. In other commercial quadrupole instruments, the accelerating voltage is applied in a two stage (telefocus) process (Wittmaack 1974). The ions are extracted by a small fraction of the accelerating voltage and then accelerated to the required energy. This method makes the source directionally stable at high energies and also prevents sputtering of the extraction electrode which can produce pitting and, after some time, arcing

between the back of the anticathode and the extraction plate. A single stage extraction system on the other hand is more stable at low extraction voltages.

In practice the source floats at the extraction potential, with the extraction aperture at zero volts for positive ions. The extraction aperture is in fact the inlet aperture to an electrostatic lens. This produces a focussed waist in the beam further down the primary ion column. The ion beam then passes through a scatter suppression aperture to eliminate any ions with trajectories that are too far off axis.

The next stage is a Wien filter which consists of crossed electrostatic and magnetic fields which mass filters the ion beam. This is to ensure that any impurities in the beam are removed e.g. aluminium ions from the ion source. The Wien filter is in fact a velocity selector but since the ions emerging from the discharge all have the same energy it acts as a mass filter. On EVA 2000 the Wien filter also contains a pair of deflection plates perpendicular to those used for mass filtering which allows for beam steering.

The beam then passes through a pressure step aperture. This a low conductance hole that enables the upper and lower halves of the ion column to be differentially pumped. The source is run at a pressure of $\approx 10^{-3}$ torr and the extraction side is at $\approx 10^{-6}$ torr. The upper ion column is pumped by a 500 l/s

turbomolecular pump and the rest of the system is pumped by an Edwards E06 diffusion pump with a Vacuum Generators CCT150 liquid nitrogen trap. The presence of the pressure step aperture enables the pressure in the main chamber to reach 10^{-8} - 10^{-10} torr during analysis.

The pressure step is also electrically floating so that the current falling on it can be measured by an electrometer. The pressure step is not an ion optical element, its only purpose is to enable differential pumping.

Following the pressure step is a set of quadrupole beam steering plates and then come two deflector plates to bend the ion beam by 2 - 4 degrees. This removes any neutral or scattered ion contaminants from the beam as they are either not deflected or not deflected enough. The neutrals could have been formed by collisions with the residual gas or recombination of ion beam species with secondary electrons generated during scattering events at any of the apertures. On EVA 2000 the bend is present only to supress scattered ions and not to remove neutrals since experiments carried out using the final lens as a electrostatic mirror showed that there was no neutral component to the primary beam (Dowsett 1988b).

Next come a set of four beam scanning plates. These are used to scan the ion beam in a raster pattern like a television picture. The beam then enters the final

Einzel lens where it is focused into a demagnified spot on the sample.

The current density profile of the spot typically has a gaussian shape with a fwhm of between 20 - 100um. In principle, the presence of the beam scanning system before the final lens introduces aberrations into the system due to the off axis deviations imparted to the beam (Liebl 1983), although this has not been observed on EVA 2000. The scan voltages can be relatively small with the scan plates before the lens since the scan plate to sample distance is large. If the scan plates were positioned after the lens then the magnitude of the scan voltage for a given scan size at the sample would be larger but the introduced aberrations would be reduced. During the course of this study the deflection system was of the quadrupole type.

2.2.2 Secondary ion column

The secondary ions sputtered from the sample have wide angular and energy distributions, and also originate from different positions on the sample. In order to collect as many of these secondary ions as possible an ion optical system called the transfer optics is used to tailor the emittance characteristic of the surface to the acceptance characteristic of the mass spectrometer. On EVA 2000 a quadrupole mass spectrometer is used. The optimum transmission and mass resolution of a quadrupole

mass spectrometer occurs when the bandwidth of the incoming ions is less than 10eV. The injection angle of the ions also affects the performance. The optimum performance occurs if the injected ions lie within a 10° cone with its apex centred ≈5mm inside the quadrupole (Wittmaack 1982a).

The transfer optics are shown in figure 2.2. It consists of the sample, extraction plate and energy filter. The sample is biased to ≈10V which ensures that the richest part of the peak of the secondary ion energy distribution is pushed into the energy window of the energy filter.

The next part of the transfer optics is the energy filter. This consists of a screening electrode with a 14mm diameter hole in it behind which is an extraction plate which has a 3mm aperture in it. The energy filter floats at a potential of ≈-200V for positive ions and this field extracts ions into the energy filter. They enter a parallel plate condenser (Wittmaack et. al. 1982b), which makes up the energy filter which is of the accel-decel type. The entrance and exit apertures of the energy filter are offset from each other, so for ions to traverse between the apertures they must be deflected. Potentials applied to the y set of plates bends ions round and those with the correct energy bandwidth will go through. The x set of plates in the energy filter act as steering plates. The exit aperture is on the axis of the

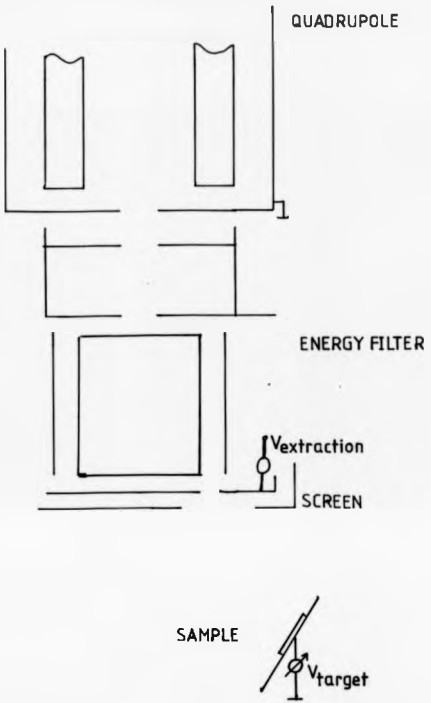

FIGURE 2.2. Schematic of EVA 2000's transfer optics, showing sample, extraction system, energy filter and the entrance to the quadrupole mass spectrometer.

quadrupole so although they have been bent they emerge on axis. Before the ions enter the quadrupole they cross a retarding field so that they enter the quadrupole with energies <10eV so that the mass resolution is increased.

The quadrupole mass spectrometer used on EVA 2000 was an Extranuclear Corporation model 162-8 with 3/8" rods operating at 3MHz or 1.5MHz during this thesis.

A quadrupole mass spectrometer works by applying a DC voltage of opposite polarities to alternate rods and superimposing radiofrequency AC voltages in antiphase to them. Ions in the quadrupole describe a complicated trajectory and only ions of one mass/charge state have a stable trajectory throughout the length of the mass spectrometer. All others collide with the rods or some other part of the vacuum system.

The ions that traverse the quadrupole then experience an accelerating potential which directs them towards the ion-electron detector.

In EVA 2000 the ion detector is a channeltron which is a curved, tapered glass tube with its internal surface covered in hydrated lead oxide. An electric field is applied along the inside of the body of the channeltron and when an ion strikes the front bell of the channeltron electrons are emitted. These are accelerated down the tube and have further collisions with the walls. At each impact ≈3 secondary electrons are emitted and the device has an overall charge gain of $\approx 10^{7-8}$ times.

External electronics amplify and count the pulses emerging from the channeltron giving the number of ions striking the detector since each pulse corresponds to one ion arriving.

In EVA 2000, pulse counting techniques are employed to enable single ions to be detected, but the upper limit on the count rate is 10^6 ions per second. For higher rates an analogue detection system such as a Daly detector could be employed using current measuring techniques.

The description of EVA 2000 given here is mainly for positive secondary ions, although negative ions can be detected quite simply although precautions have to be taken to prevent secondary electrons giving spurious counts. This is done by producing a magnetic field in the vicinity of the exit aperture of the quadrupole to deflect electrons away from the channeltron.

2.3 Control Electronics

EVA 2000 is controlled by a Research Machines Limited 380Z microcomputer. The instrumental parameters that are under computer control are mass,target potential, beam on/off, primary energy on/off, sample holder position and raster size. The computer also controls the pulse counter by implementing the electronic gating. All beam set up parameters, the source settings and energy filter settings are controlled manually.

The raster scanner that produces the sweep signals for the ion beam also drives a storage oscilloscope with the intensity being driven by an analogue ratemeter which receives the input pulses in parallel with the digital pulse counter. One complete scan of the raster scanner is called a frame.

Existing electronic raster scanners are based on digital electronics that produce a 256 x 256 point raster. Digital rather than analogue electronics are used in order that electronic gating can be easily incorporated. Electronic gating ensures that ions are detected only when the ion beam is in the centre of the crater and thus avoids the detection of any secondaries produced from the crater walls (Wittmaack 1976).

Electronic gating is not the only way to ensure that ions from the crater edges are rejected. On magnetic sector instruments the secondary column is designed to form images in certain planes in which apertures can be placed to limit the field of view (Slodzian 1983). If the total scanned area is larger than this then any crater edge effects are eliminated by this 'optical gating'. Some instruments can also have a combination of optical and electronic gating giving even greater rejection of stray ions. Another method of gating has been incorporated into a new commercial SIMS instrument (VG Microtrace IX70S). Here, the secondary ion beam is

blanked when the primary beam is outside the gated area, the instrument also has optical gating.

With the advent of cheap semiconductor memory devices another form of gating - digital gating - can now be considered. If the ion beam is slowly stepped one pixel at a time, then a two dimensional picture can be built up showing the surface intensity of the species of interest. If all the images are stored, then, at the end of the profile a series of images of the sample corresponding to slices through the original sample are obtained. The digital gate can now be applied. If it is placed centrally and all the data points within it are summed then the result will be the same as with traditional electronic gating. By moving the gate around, information about the lateral distribution of dopants can be obtained.

Also, if a surface contaminant is observed, say a lump of alumina on the surface of a silicon on sapphire sample, then the digital gate can be moved so as to remove it from the data to be summed, whereas, with electronic gating there would be no option but to repeat the experiment.

Microprocessor control of raster scanners means that the sweep function generated need not be a simple sawtooth waveform, but can be swept in a 'random walk' about the surface. The beam could also be moved in surface covering patterns, where the beam never crosses

itself but still covers the whole surface, hence removing any problem associated with flyback pulses. However this will cause other problems. In a system that uses a staircase waveform, any time of flight or electronic delay effects are constant for each point on the scan (Wittmaack 1980). If a different scan waveform is used, then the effects mentioned could lead to image doubling or other non-registration effects that would need sophisticated computer processing to remove.

2.4 Software

All the instrumental software interfaces are written in machine code subroutines that can be accessed by BASIC. This enables anyone to write a program to operate the SIMS instrument without knowing the details of the hardware/software interface (Dowsett et.al. 1985).

The depth profiling software in general use is DEPRO. This enables the user to set up to nine mass channels with associated target potentials and target potential break points, a series of raster sizes and also mass offsets if required. All this initialization information is saved on disc so that the settings can be reloaded for another profile. Once the profile has started the computer sets up all the relevant masses and potentials at the start of a scan, or frame, so that all the parameters are set up before the ion beam reaches the gated area.

It does this for all the mass channels in turn until the user terminates the profile. The program outputs the data in printed form and also as a graphical plot. At the end of the profile the data is saved onto disc. A depth profile may be interrupted to allow mass and/or energy spectra to be obtained without losing depth calibration.

Versions of DEPRO also exist for overnight running, which turns the ion beam and accelerating potential off at the end of the experiment, and for batch running when a stepper motor connected to the sample manipulator translates samples in front of the ion beam to enable up to 10 samples in succession to be analysed without operator interaction. A program to drill craters for a certain number of frames is also available. Mass and energy spectra of samples can also be obtained by using dedicated software to perform these tasks.

2.5 Post Analysis Processing

A SIMS depth profile produces data in the form of a table of intensity versus time. This has to be transformed into the form of concentration against depth.

The depth calibration is obtained by measuring the the depth of the sputter crater using a DEKTAK surface profilometer.

A program called PROED (Dowsett 1982) is used to quantify the data from a depth profile. By inputting the

measured depth, the program calculates the sputter rate for the profile, taking into account any changes in raster size. If the sample contains more than one matrix, i.e. SiO_2 on Si then further corrections to the depth scale must be made.

The concentration scale can be quantified in a number of ways. If a sample of known concentration is analysed before the unknown sample then the calibration constant that is used to convert from intensity (counts/frame) to concentration can be used for the unknown sample. This is the external standard method and the standards used are ion implants.

PROED contains a subroutine to calculate the calibration constant for an implant given the ion dose. Another method of calibration is to use the relative sensitivity factor. This is obtained by comparing the intensity of a matrix channel to the desired channel in a standard. This again gives a calibration constant for the system under analysis. This number should be the same for an unknown sample of the same system. It is important to recalculate the calibration factor for each matrix/impurity combination.

The software also allows for corrections for some of the problems associated with SIMS depth profiling of semiconductors. These include different sputter rates for different matrices, the differential shift (Chapter

4) and finding and subtracting background signals from the profile.

Also included are presentation features such as interpolation, so that the data are given in equal depth increments. A N point running average can be used to smooth the data. Inter channel arithmetic can be used to ratio the data from different channels and data parameterization to give moments (chapter 3), decay lengths and full and half widths of profiles.

Originally, PROED was written in BASIC to run on a Digital Equipment Corporation DEC10 computer. Subsequent versions were written for a VAX 750 and a Research Machines Nimbus as the computing facilities changed. Each translation introduced new features to take the enhanced capabilities of each computer into account. For example, running PROED on the Nimbus enabled a graphic display routine to be written so that the depth profile could be displayed during data analysis for the first time.

However, BASIC on the Nimbus was found to be too slow for the kind of data that was being routinely processed. Hence I rewrote the program in FORTRAN to increase the speed of execution. This also afforded an opportunity to correct the bugs that had crept in during five years of continual development. The final FORTRAN version now runs up to 25 times as fast as the BASIC

version, which provides the enhanced data handling capacity that is now required.

PROED can also analyze data in formats other than that produced by EVA 2000. On EVA 2000 it is assumed that each channel in a depth profile is acquired for the same period of time, i.e. one frame. On a magnetic sector instrument such as the IX70S, it is possible to acquire data for different lengths of time for each channel. This enables the species of interest e.g. boron, to be acquired for a different length of time than the matrix channel, which is only used for diagnostic purposes. In this case boron could be acquired for ten seconds and silicon, the matrix channel, for one second.

Previously, this would have meant the relative positions of the data points would have been incorrect after processing, but this has now been allowed for.

If in the future different data formats are required, then it is a simple task to incorporate them into the software by either adding a subroutine to take this difference into account, or, adding a 'front end' to the software that converts the data to EVA 2000 format.

2.6 Conclusion

EVA 2000 is a computer controlled quadrupole SIMS instrument which is UHV compatible. Since this project finished it has been upgraded to include 3/4" inch quadrupole rods which increased the transmission of the

instrument by a factor of 10. Also incorporated is a secondary electron detector so that images can be rapidly obtained to assist with primary beam focussing. The final lens has been changed from an assymmetric Einzel (Septier) lens to a symmetric lens that has the same power as the old lens, but occupies half the volume (Dowsett et. al. 1985). The scan plates have been positioned after this lens and split into seperate x and y plates.

Software changes now allow the x and y sizes of the crater to be independantly variable and a software zoom function has been added to enable beam focussing to be simplified.

CHAPTER 3

DATA ANALYSIS

3.0 Overview

In this chapter the need for a method of parameterizing ion implants is discussed. A method of doing this , constructing Pearson distributions, is investigated. The validity of using curves constructed from four moment data is discussed. The results of this investigation were compared with results published in the literature. Finally the use of the parameters derived from the four moment data only, is propounded as a reliable method of describing implant profiles obtained by SIMS without the need to construct a distribution.

3.1 Introduction

In order to obtain some measure of the trends in an implant distribution, for example ion ranges into different matrices, diffusion coefficients for process models or just general parameters for inter-laboratory comparison of data, it is necessary to use a reproducible method for identifying features of an implant profile. There are two methods that can be used: Either to establish the peak position by visual inspection, i.e. finding where the tangent to the profile is parallel to the x-axis, or by mathematical means. However, it is

difficult to find the maximum in even slightly noisy data and it is necessary to fit a function through part of it.

Visual inspection can introduce appreciable errors into the measurement due to uncertainties in the peak shape. Therefore, it was decided to mathematically represent the data by taking moments and then constructing a distribution. Various distributions have been used to represent implant profiles. These include a Gaussian, two half Gaussians back to back, Edgeworth and Pearson IV curves. It was decided to investigate Pearson distributions since a number of people (Hofker et.al. 1975), (Ryssel 1980) have used Pearson IV curves to model implant profiles and have claimed exellent results (Sze 1983).

Current stopping theory (Lindhard et.al. 1963) derives the first four moments of the implant as part of the method. Therefore constructing a theoretical distribution based on the first four moments of the measured implant seems a reasonable thing to do.

When determining the goodness of fit - whether by mathematical means, or by eye, it is necessary to decide which parts of the depth profile should be included. A boron depth profile, under oxygen bombardment, always exhibits a surface spike. The spike is caused by drive in of surface impurities during ion implantation. This contamination could have come from previous processing

steps such as heating in a vacuum system with borosilicate glass viewports (Kubiak et.al. 1986).

This spike often has a maximum concentration greater than that of the implant itself. If this feature was included in the goodness of fit calculation, then it would weight the fitted curve away from the actual implant shape.

In practice, the decision as to whether or not to include the surface spike can be made by examining the isotope ^{10}B. If only boron-11 was implanted any boron-10 in the surface spike region was present before implantation. The boron-11 present before implantation can be subtracted from the spike by using the $^{10}B/^{11}B$ ratio.

In arsenic profiling, the surface transient builds up exponentially from a low level. This would effect a variance calculation by pulling the constructed curve below the actual profile.

Both the above situations call upon the experimenter to exercise judgement as to whether the features observed in the near-surface region should be included in the calculation or not. Therefore in this preliminary study the goodness of fit was judged by eye, a method that has been used in the literature (Hofker 1975).

The Pearson series of curves were invented by Karl Pearson in 1924 to describe frequency distributions. The original use of Pearson's system of frequency curves was

in the actuarial profession where they accurately represented the mortality distribution of a population. However, in practice, actuaries use whatever system of curves will give a good fit to the data. There is no a-priori reason why the Pearson curves themselves should be used over any other distribution (Leighton 1987).

3.2 Pearson's system of curves

Pearson curves are solutions to the hypergeometric equation

$$\frac{1}{y}\frac{dy}{dx} = \frac{(a + x)}{b_0 + b_1x + b_2x^2} \qquad 3.1$$

To get the equation in the form y=f(x) the right hand side of 3.1 needs to be integrated and the integral depends on the roots of the quadratic equation in the denominator. The coefficients a, b_0, b_1 and b_2 can be determined from the moments of the distribution. The moments are defined by

$$\mu_1 = \int_{-\infty}^{+\infty} x\, f(x)\, dx \qquad 3.2$$

and

$$\mu_n = \int_{-\infty}^{+\infty} (x - \mu_1)^n\, f(x)\, dx \quad n = 2,\ 3,\ 4 \qquad 3.3$$

where f(x) satisfies:-

$$\int_{-\infty}^{+\infty} f(x)\,dx = 1 \qquad 3.3a$$

the parameters are obtained from the moments by

$$\text{mean} = \mu_1 = R_p \qquad 3.4$$

$$\text{standard deviation} = \sigma = \sqrt{\mu_2} \qquad 3.5$$

$$\text{skewness} = \tau = \mu_3/\sigma^3 \qquad 3.6$$

$$\text{kurtosis} = \beta = \mu_4/\sigma^4 \qquad 3.7$$

Where R_p is the projected range for an implant. The skewness is a measure of the assymmetry of a distribution and the kurtosis is a measure of the flatness of the peak shape. A Gaussian curve has a skewness of zero and a kurtosis of three. Both skewness and kurtosis are dimensionless quantities, whereas, μ_1 and σ have units of length.

The coefficients can be obtained from the parameters by

$$a = \frac{-\sigma\tau(\beta + 3)}{A} \qquad 3.8$$

$$b_0 = \frac{-\sigma^2(4\beta - 3\tau^2)}{A} \qquad 3.9$$

$$b_1 = a \qquad 3.10$$

$$b_2 = \frac{-(2\beta - 3\tau^2 - 6)}{A} \qquad 3.11$$

where

$$A = 10\beta - 12\tau^2 - 18 \qquad 3.12$$

The criterion $k=b_1^2/4b_0b_2$ determines the roots of the quadratic. If k is negative then the roots are real and of opposite sign. If k is positive and less than one then the roots are complex. If k is greater than one then the roots are real and of the same sign.

These roots give rise to Pearson curves of type I, IV and VI respectively. The remaining nine types are limiting cases of the above three (Elderton et.al. 1969).

The solution to 3.1 when the quadratic has complex roots gives the equation for a Pearson IV :-

$$\ln y = \frac{1}{2b_2} \ln (b_2x^2 + b_1x + b_0) + \frac{2a - b_1b_2}{\sqrt{4b_0b_2 - b_1^2}} \tan^{-1} \frac{2b_2 + b_1}{\sqrt{4b_0b_2 - b_1^2}} \qquad 3.13$$

The various Pearson curves can be U shaped, J shaped or bell shaped. The Pearson IV curve is a unimodal bell shape curve with unlimited range in both directions, which is clearly different from a real implant.

3.3 Software

A computer program was written in FORTRAN on the Research machines Nimbus computer to construct a Pearson IV distribution from the moments of experimental data.

The program was used to read in a data file from a 10^{15} cm^{-2} 150keV germanium implant into silicon (Dowsett 1987).

It first calculated the moments of the data and then constructed a Pearson IV solution and displayed the data and the fitted curve on the monitor screen, this is shown in figure 3.1. The fit is good in the leading edge region but in the peak and trailing edge region there is a significant deviation. The peak position of the fitted curve is nearer to the surface than that of the data.

The program was then altered so that the parameters could be entered manually. If the value of k indicated that the parameters were not consistent with a Pearson IV solution then the program prompted for a new input. This procedure was repeated until the fit was judged to be satisfactory. This is the same procedure as used in the literature (Hofker 1975), (Vandervorst et.al 1984). With experience, a good fit could be obtained after just five repetitions. The output after this procedure is shown in figure 3.2. Although the trailing edge is better, this is at the expense of a worse fit in the leading edge region. More importantly, this involved changing the projected range from 0.252 to 0.254μm, the standard

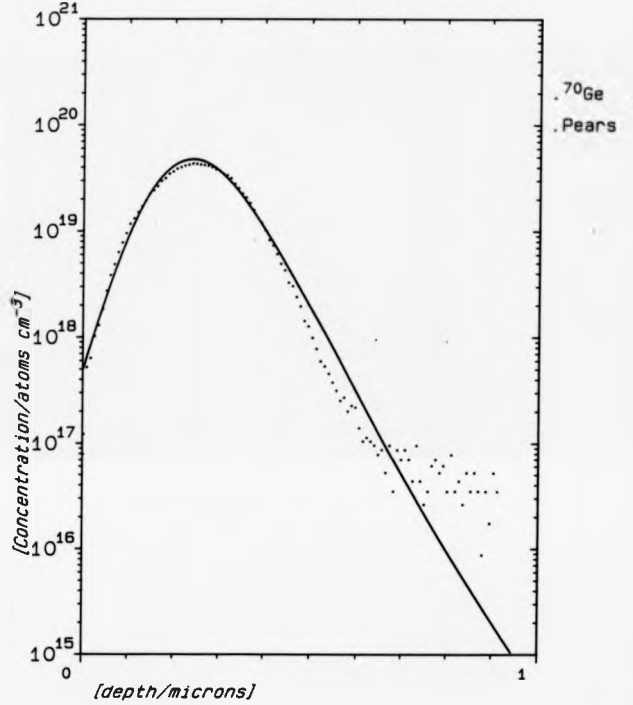

FIGURE 3.1. Pearson IV distribution fitted to a 150keV ^{70}Ge implant using the moments of the data.

deviation from 0.0909 to .0838μm, the skewness from 0.449 to 0.237 and the kurtosis from 3.944 to 3.279. Now, changing the moments in order to give a good fit gives no information about the original implant. It only gives information about the curve which is not the object of the exercise.

For comparison, the program also used the first two moments to generate a Gaussian distribution to fit the data, figure 3.3. This is a better fit than either of the Pearson attempts and the deviation from the data in the trailing edge region is just due to a channelling tail. The program was used to calculate the moments of a series of shallow implants into crystalline silicon, silicon pre-amorphised by a high dose self implant and silicon dioxide (see table 4.1). Out of twenty seven profiles only one, arsenic into SiO_2 analysed at 4keV, gave moments that would have enabled a Pearson IV to be constructed. All of the other results indicated that a curve of Pearson type I should be used since k was negative.

3.4 Analysis

Stopping theory calculations indicate that the use of four moment data for quantifying implant profiles is valid, but the type of curve used to actually fit the data is a matter of artistic judgement. (Ziegler et. al. 1985).

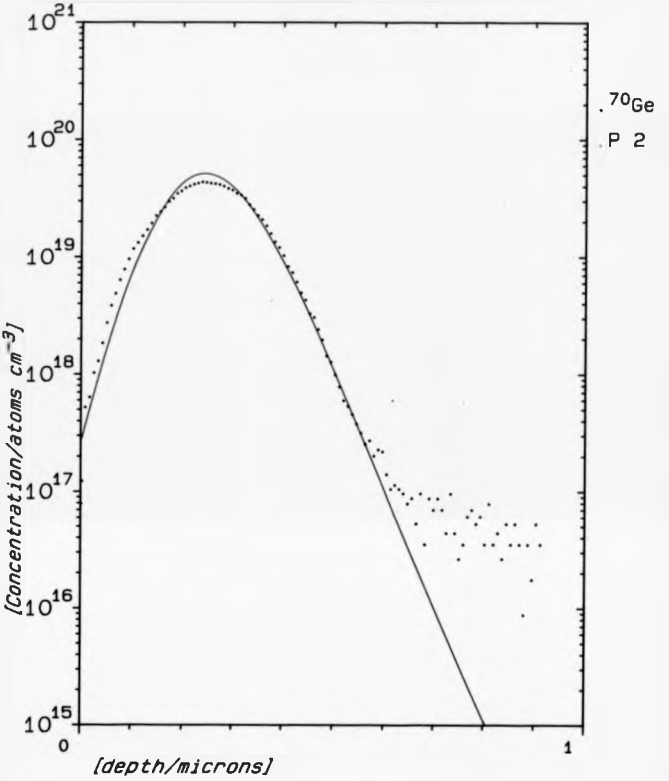

FIGURE 3.2. Pearson IV distribution fitted to the same implant data as figure 3.1, using moments estimated to give best fit.

The expressions used for calculating the moments 3.2, 3.3, contain an integral from minus infinity to plus infinity, whereas, an implant extends only from the surface (zero) to a finite depth. The difference between these ranges is enough to explain the discrepancy between the calculated curve and the data.

In a low energy, i.e. shallow, implant, the surface concentration of the implanted species is a significant fraction of the maximum concentration. Therefore, a curve calculated using the moments of the implant will extend some way into the minus x direction, and the presence of this region will cause the mean of the curve and hence the other moments, to be smaller than those of the data. However, for a high energy, i.e. deep, implant the surface concentration is very much smaller than the peak concentration. This means, that the contribution to the mean position of the calculated curve from the negative x region will be negligible and hence, the moments of the fitted curve and the data will be almost the same.

Therefore, since the closeness of fit depends on the energy and type of the implant, actually calculating a curve to fit the data is a very hit and miss affair and does not give any benefit. However, the process of taking moments to characterize the data is correct, whatever the implant conditions.

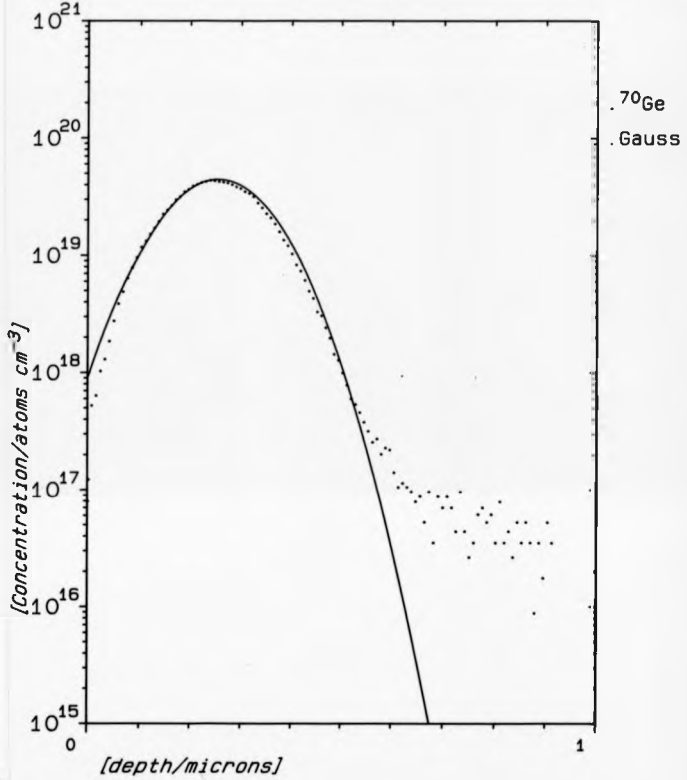

FIGURE 3.3. Gaussian distribution fitted to Ge implant data using the first two moments only. Note the fit in the peak region is better than either figure 3.1 or 3.2.

Thus using moments to characterize the data gives a reproducible method of analysing an implant, which curve fitting does not.

3.5 Conclusion

The fitting of any analytical function to a SIMS depth profile of an implant by taking moments, although possible does not give any information about the original data. This is because the moments of the calculated curve cover a different range to that of the data.

Therefore, in order to characterize a depth profile, no attempt is now made to construct an analytical function, since this has been shown to be invalid. Instead the moments of the data are taken and they are used as a reproducible way to represent the profile. Instead of using the peak position or mode, the mean is used since this corresponds to the projected range given in ion range tables.

It has been said that 'only Pearson IV solutions are applicable to implanted profiles' (Siedel 1983). Hofker has correctly shown that the three main types of Pearson curve, I, IV and VI are all applicable since the type depends on the value of k. The assumption about the applicability of Pearson IV curves may arise from an incorrect belief that Pearson IV curves are the only ones to have four moments. This is highlighted by the paper by Vandervorst, which shows an arsenic implant profile

which has had a Pearson IV distribution fitted to it. The parameters extracted from the data are given and the skewness and kurtosis are given dimensions of length, but these are dimensionless constants as noted above. In the book VLSI Technology edited by Sze (McGraw-Hill 1983) there is a table of moments for B, P, As and Sb implanted into poly-crystalline silicon at four different implant energies (Seidel 1983). These were used to fit a Pearson IV curve. Using equations 3.8 - 3.12 the value of k was calculated to see if a Pearson IV solution was indeed correct.

OUT OF SIXTEEN EXAMPLES SEVEN WERE NOT PEARSON IV AND OF THE REST ONLY THE PHOSPHORUS DATA GAVE PEARSON IV FITS ACROSS THE RANGE OF IMPLANT ENERGIES USED.

The ability to take moments of profile data has been incorporated into the data processing software used by the SIMS group at Warwick to enable characterization of implant profiles to be carried out.

CHAPTER 4

DIFFERENTIAL SHIFT MEASUREMENTS

4.0 Overview

This chapter describes a series of experiments to determine the magnitude of the differential shift in three different technologically important materials for a range of commonly used dopants. The data analysis techniques described in chapter 3 are used to measure the differential shift. The existence of the pre-equilibrium variation in the ion signal led to the use of Si-MBE grown amorphous capping layers to allow the pre-equilibrium intensity variation to finish before the implant was profiled. The different behaviour of the three dopants will also be discussed.

4.1 Introduction

At the beginning of a SIMS depth profile there are, of course, no primary beam atoms present in the sample. As the profile proceeds the concentration of the primary species increases, until, after a period of time, the number of primaries present in the sample comes into steady state with the primary beam, where the number of primaries being sputtered equals the number of primaries being incorporated (Williams 1979), (Clark et.al. 1989). The period before a steady state is established is referred to as the pre-equilibrium region.

The width of the pre-equilibrium region in time is dependant on the primary ion energy, since, the higher the energy the larger the projected range and the larger the standard deviation about it of the ions into the sample. This means that for a given current density it takes longer for for the altered layer to form since it occupies a larger volume of material (Clark et.al.1988).

The presence of this pre-equilibrium region gives rise to two significant problems in the analysis of shallow features:

i) The sputter rate changes as the number of primaries being sputtered increases giving rise to an effect called the differential shift (Wach et.al. 1981).

This occurs if a constant sputter rate is assumed when calibrating the depth scale of the data, giving an apparent shift in the depth of a feature due to the actual change in the sputter rate in the pre-equilibrium region. This shift is only noticeable if the sample is analysed using different primary beam energies, since the width of the pre-equilibrium region is primary ion dependent.

ii) The secondary ion yield also changes in the pre-equilibrium region, due to variations in the chemical environment of the near surface atoms. This variation makes the quantification of shallow features very difficult as well as distorting the feature shape (Wittmaack 1975).

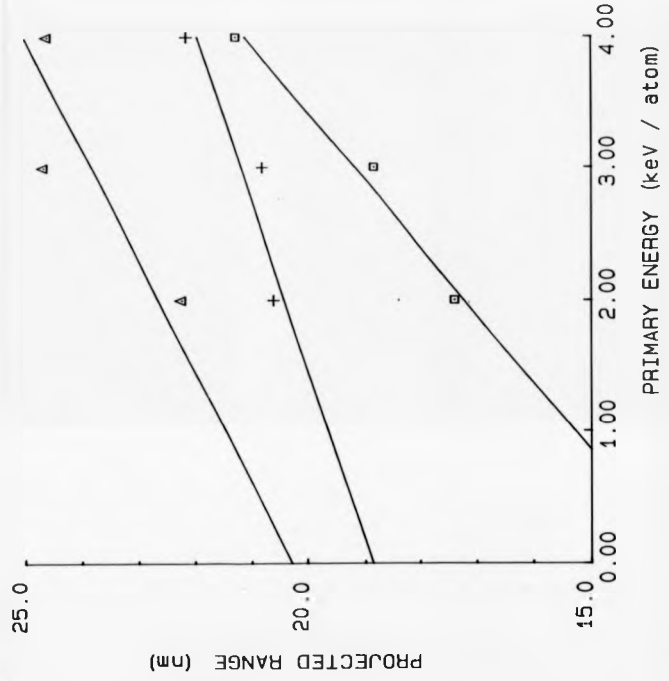

FIGURE 4.1. Position of projected range against primary atom energy for uncapped implants into silicon. Boron - crosses, Phosphorus - triangles, arsenic - squares. The lines are drawn to guide the eye only.

The differential shift can be corrected for but it is necessary to evaluate it for each different matrix encountered. In this investigation three technologically important matrices were used. Crystalline silicon, silicon that had been pre-amorphised by a high dose self implant and silicon dioxide.

Pre-amorphisation is used to reduce the amount of channelling during the implantation process and also to enhance the amount of diffusion, in the damaged region, during the following annealing stage (Godfrey et.al 1985).

It was decided to measure the differential shift in various matrices for various impurity species with the intention of correcting for it when calibrating the data.

4.2 Experimental

To investigate the differential shift $^{11}BF_2$, ^{31}P and ^{75}As were implanted into three technologically important materials: crystalline Si, Si which had been pre-amorphised with a high dose self implant and thermally grown SiO_2. The implant energies were 20 keV for BF_2 and As and 15 keV for P. BF_2 was used so that the implanter could be run at higher energies whilst still giving a very shallow B implant. There were two reasons for doing this: Firstly, at higher beam energies a larger beam current can be used which minimises dose fluctuations between different samples. Secondly, the geometry of

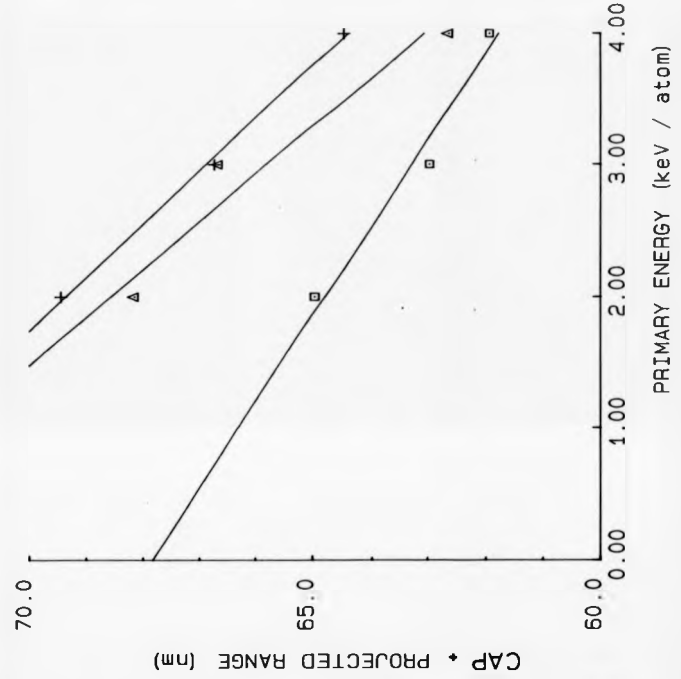

FIGURE 4.2. Position of projected range below surface of capped sample against primary atom energy. Boron - crosses, Phosphorus - triangles, arsenic - squares. The lines are drawn to guide the eye only.

many commercial ion-implanters is such that the miminum ion energy that can be used is 10keV. Thus, in order to use a lower implant energy a second, deceleration stage must be incorporated into the beam line, causing considerable down time and increased expense. A 20keV BF_2 implant is assumed to be equivalent in terms of boron range to a 4.5keV boron implant. The implants were made at doses of 10^{14} and 10^{15} atoms cm^{-3}. Two wafers were implanted for each substrate/dose combination.

The high dose crystalline Si wafers had 500Å silicon caps grown on them by silicon molecular beam epitaxy after ion implantation. This was done in our Vacuum Generators V80 Si-MBE machine without heating the substrate so that no epitaxial growth took place.

The capped layers were used to ensure that any variation in secondary ion yield in the pre-equilbrium region occured before the implant was reached, thus removing the second quantification problem mentioned above.

The SIMS depth profiles were performed on EVA 2000 with O_2^+ primary ions at normal incidence with energies of 4, 6, and 8keV and a fixed beam current of 200nA. The depth of the craters were measured after analysis on a Sloan corporation Dektak 3030 Auto II.

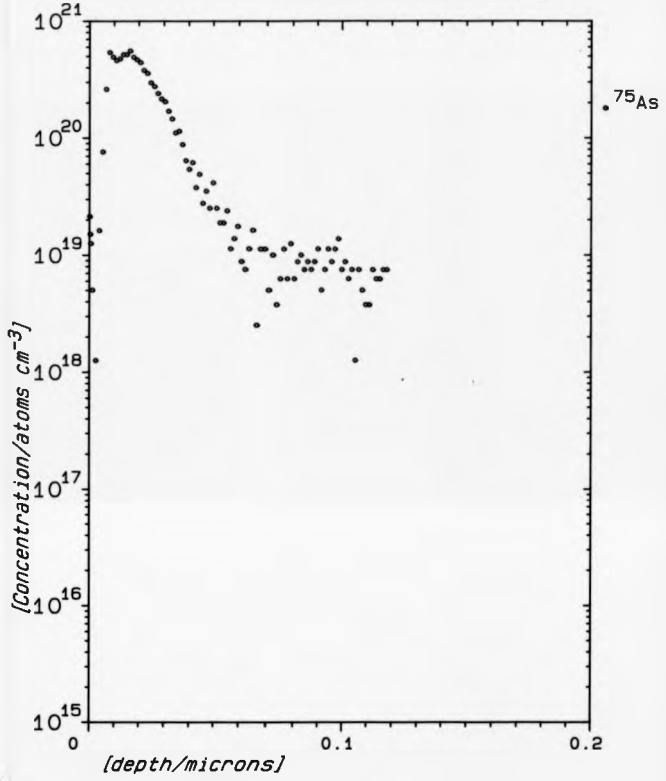

FIGURE 4.3. Depth profile of 10^{15}, 20keV arsenic implant under 8keV O_2^+ bombardment, showing arsenic spike in the leading edge due to segregation.

4.3 Results

Studies (Augustus et.al. 1988) have shown that the thickness of the altered layer in Si bombarded by 4keV O_2^+ at normal incidence is 20nm. Ion stopping calculations show that the projected range of a 20keV As implant is 19.2nm, of a 15keV P implant is 22.6nm and the range for boron of a 20keV BF_2 implant is 18.8nm. Therefore, most of the leading edge of the implant is contained in the pre-equilibrium region and so the quantification of this region is made very difficult. Shallow implants were used to emphasise this problem.

Finding the mean of the data by taking moments (see chapter 3) and plotting the mean against primary ion energy for the crystalline samples gives the graph shown in figure 4.1. The differential shifts were 0.77nm/(keV/atom) for boron, 1.18nm/(kev/atom) for phosphorus and 1.94nm/(keV/atom) for arsenic. The mean position appears to move further into the sample as the primary ion energy is increased for each of the three implanted species.

The equivalent data for the capped crystalline samples is shown in figure 4.2. The differential shifts were -1.5nm/(keV/atom) for arsenic, -2.4nm/(keV/atom) for boron and -2.7nm/(kev/atom) for phophorus. This minus sign indicates that the apparent shift was towards the surface as the primary ion energy increased.

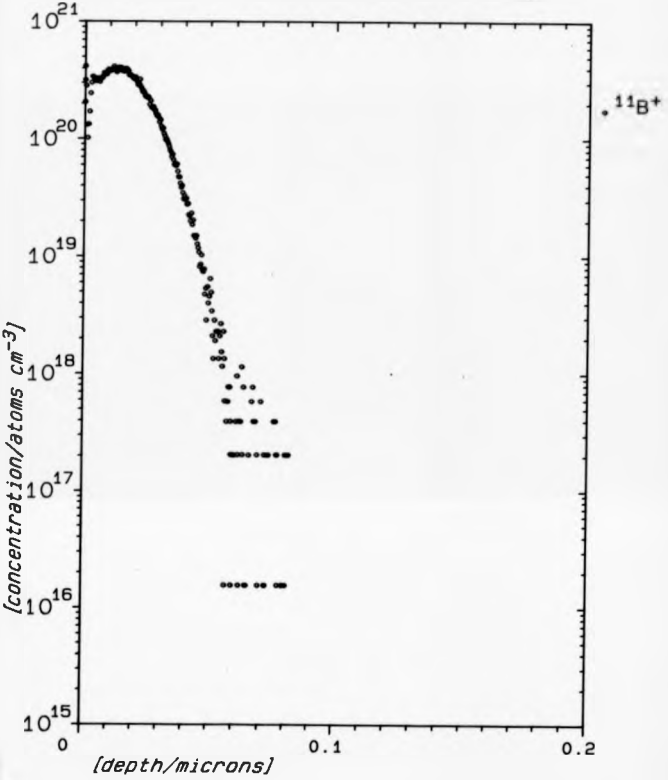

FIGURE 4.4. Depth profile of 10^{15}, 20keV BF_2 implant under 2keV O_2^+ bombardment.

Neither the amorphous or the oxide samples exhibited any consistent behaviour and this may again be due to to the effect of the pre-equilibrium region. However with these samples it was not possible to grow capping layers and investigate this further. The complete set of data including the Pearson calculations is shown in table 4.1.

4.4 Discussion

In the pre-equilibrium region, the secondary ion yield is reduced and thus the mean of the data appears to be shifted away from the surface. As the primary ion energy is increased this shift gets larger as more of the implant lies within this region.

Figure 4.3 shows the depth profile of the uncapped arsenic sample under 8keV ion bombardment. The leading edge of this profile shows a spike 8nm below the surface. This indicates that segregation of arsenic behind an oxide layer took place.

Silicon that is exposed to air will rapidly grow a thin native oxide (Frantsuzov et.al. 1976). As depth profiling begins an oxygen implant will start to be made at a depth characteristic of the bombardment energy. For 8keV O_2^+ this depth will be ≈30nm i.e. behind the surface oxide. As bombardment continues the oxygen concentration in the material increases until stoichiometric SiO_2 is formed. Further bombardment causes the atoms to migrate to the wings of the implant where unreacted silicon is

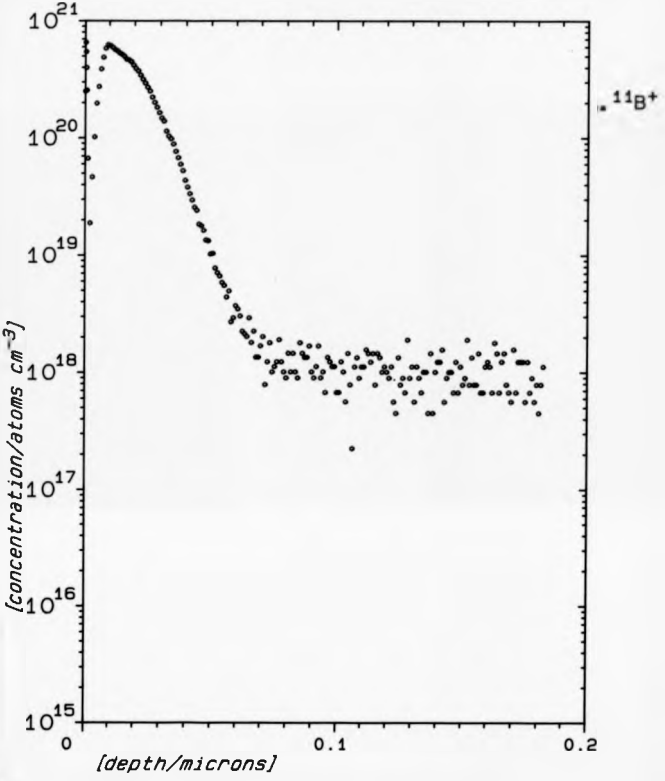

FIGURE 4.5. Depth profile of 10^{15}, 20keV BF_2^+ implant under 8keV O_2^+ bombardment, showing the variation of the boron signal in the pre-equilibrium region.

present (Littlewood et. al. 1988). The net effect of this is that an oxide layer is formed beneath the native oxide at the surface. Any arsenic in this region will be pushed in front of the growing oxide and move towards the surface. Near the surface it meets the back of the native oxide and the arsenic accumulates there. When the instantaneous surface breaks through the native oxide, the accumulated arsenic is sputtered giving a much higher signal than expected, hence the spike observed.

If higher bombardment energies are used then the arsenic spike should be larger since more of it accumulates as the initial implantation depth is deeper.

This segregation effect explains why the slopes of the lines in figures 4.1 and 4.2 are different for the capped and uncapped layers.

In the capped layers the apparent outward differential shift was countered by a smaller inwards shift caused by segregation. This had the net effect that the arsenic differential shift appears smaller than that of boron.

In the uncapped layer the inward shift due to the supressed ion yield in the pre-equilibrium region adds to the inwards segregational effect and the arsenic differential shift appears to be greater than that of boron.

In both the capped and uncapped layers the displacement between the different species is due to the

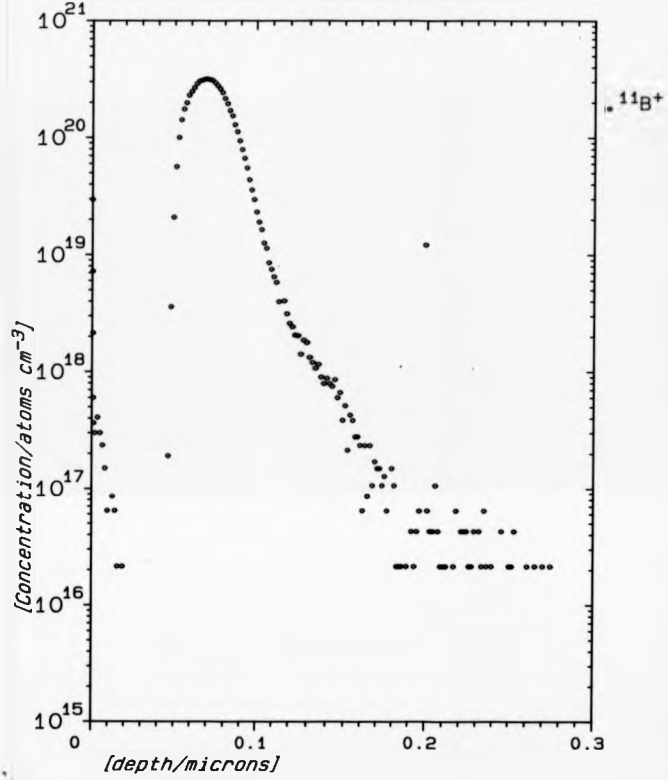

FIGURE 4.6. Depth profile of 10^{15}, 20keV BF_2^+ implant into capped layer under 2keV O_2^+ bombardment.

different ranges of the ion implants and thickness of the caps.

The profiles shown in figures 4.4 and 4.5 show the boron profiles for 2 and 8keV bombardment respectively. They show the difference in the leading edges of the implants due to the different altered layer thicknesses. This is why the differential shift for the uncapped layers appears to be away from the surface. The intensity of the boron signal under 8keV bombardment is much lower than that of the 2keV profile. This has the effect of weighting the first moment calculation away from the surface.

When the experiment was repeated with the capping layer, figures 4.6 and 4.7, it can be seen that the profiles appear identical since the since the ion yield variation due to the pre-equilibrium region has been remaved from the vicinity of the leading edge of the implant.

The same effect could have been achieved by using an implant of higher energy where the high concentration regions which have the most effect on the determinatiomn of the moments would again be away from the pre-equilibrium region.

Wach et.al. found that the differential shift of a 10keV boron implant into silicon was -1.4nm/(keV/atom). The difference between this result and that obtained here is due to the fact that that the pre-equilibrium region

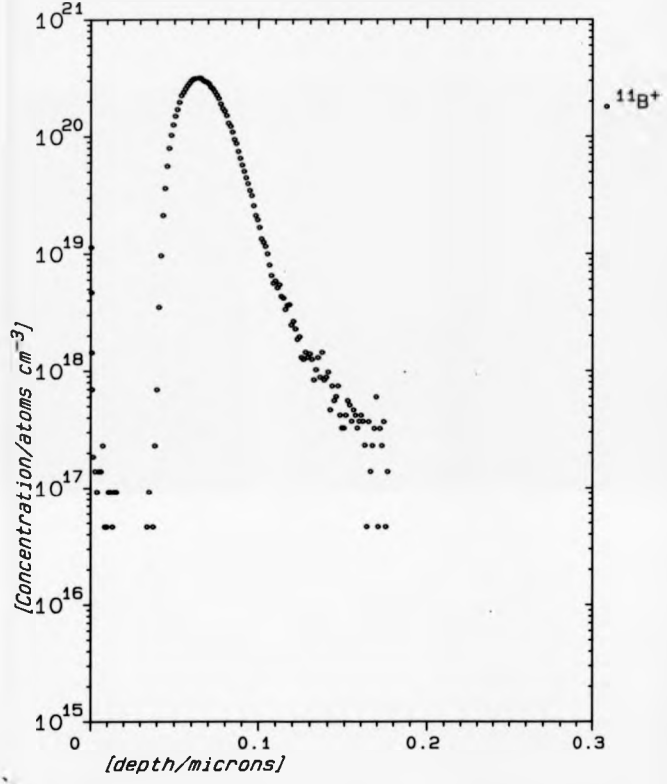

FIGURE 4.7. Depth profile of 10^{15}, 20keV BF_2 implant into capped layer under 8keV O_2 bombardment. This profile has no distortion in the leading edge unlike figure 4.5, also the profile is the same shape as figure 4.6.

affected the secondary ion yield in the same manner as for the uncapped layers, but not to the same extent, since the range of a 10keV boron implant is twice that used here. Therefore, although there were the same two competing processes as above, the inward effect of the ion yield variation just reduced the outward effect of the differential shift.

Capping layers have been used before to look at surface impurities on silicon (Williams et.al. 1980), (Slusser 1985), where the overlayers were vapour deposited polysilicon. In our case, the layers were amorphous silicon grown by molecular beam epitaxy without heating the substrate. This room temperature growth led to surface impurities being buried at the interface. Predominant among these were water related reaction products. In consequence, the phosphorus profile, figure 4.8 shows a kink in the leading edge. A depth profile of the boron implanted sample also looking at mass 31 and mass 1, figure 4.9, shows a distinctive broadening by atomic mixing of a layer of impurity trapped at the interface. Thus the kink in figure 4.8 was caused by a mass interference between ^{31}P and $^{30}Si^{1}H$ which cannot be resolved by a quadrupole mass spectrometer. Repeating the analysis with an instrument with a high enough mass resolution, e.g. a magnetic sector instrument, would remove this interference.

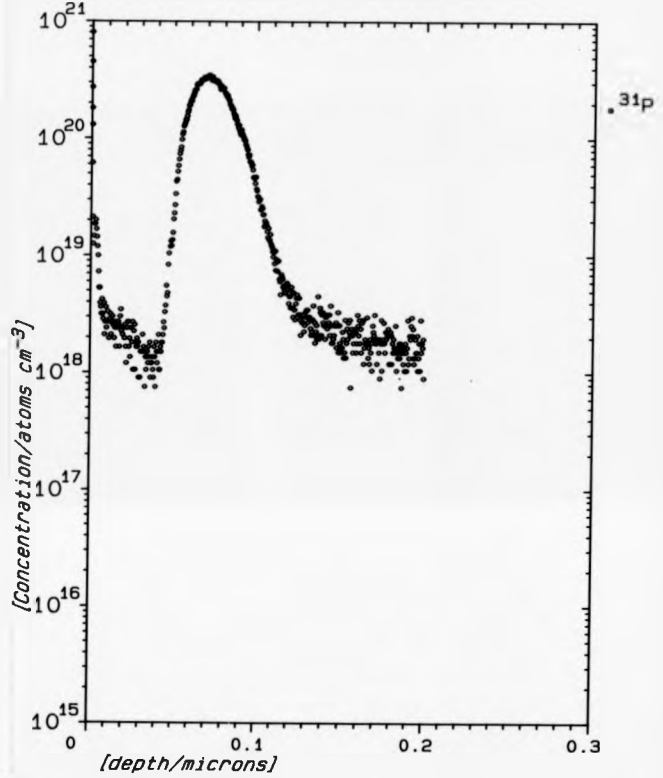

FIGURE 4.8. Depth profile of 10^{15}, 15keV P implant into capped layer under 4keV O_2^+ bombardment, showing a kink in the leading edge.

If the substrate was heat treated before MBE growth then the water and other impurites would be driven off (Houghton et.al. 1987). If heat treatment was used then there would be no reason why epitaxial growth could not also be attempted, although in either case the effect of elevated temperature on the implant would have to be investigated first.

4.5 Conclusion

In chapter 3 the technique of taking moments to characterize implant profiles was discussed. This method has been used to investigate the differential shift of three implanted species into silicon.

When investigating shallow features by SIMS it is important to take into account how much of the data will be distorted due to the pre-equilibrium region's affect on the secondary ion yield. One way to get round this is to cover the sample with an overlayer of the same matrix material. This ensures that the variation in secondary ion yield has finished before the feature of interest is reached. However, the effect of the sputter rate change is still present and will effect the depth calibration. This can be removed during data processing by adding the amount of the differential shift to the depth scale. For a deep implant the peak would appear to move towards the surface, but other parts of the implant would be shifted in or out depending on where they are.

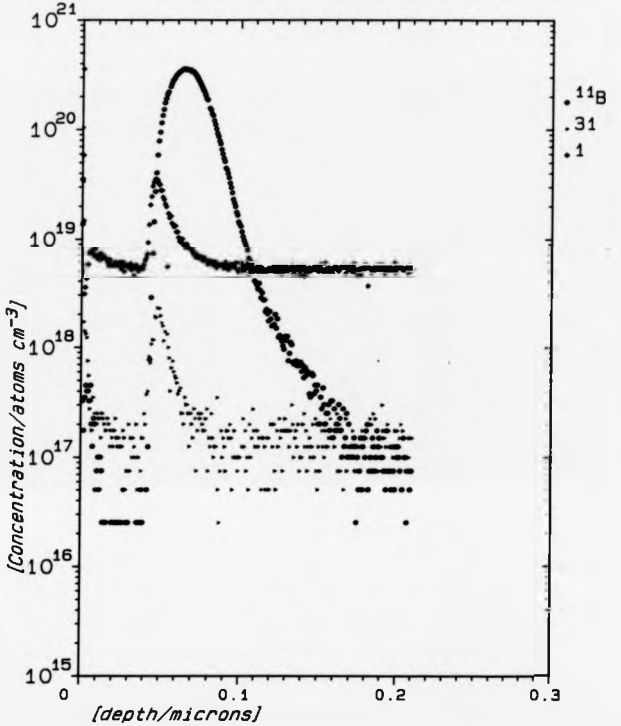

FIGURE 4.9. Depth profile of 10^{15}, 20keV BF_2 implant into capped layer under 4keV O_2^+ bombardment. This sample was also profiled using channels at mass 31 and mass 1. There is a peak at the interface for both these channels due to impurities incorporated during growth of the capping layer. These peaks have the characteristic shape of an atomically mixed layer, figure 1.3.

The presence of segregation effects when depth profiling for arsenic with normal incidence O_2^+ bombardment prevents an accurate determination of the differential shift being made, since the segregation effect is included in the measurement. If non-normal incidence bombardment conditions were used, then this effect would be removed, since SiO_2 is not formed. This would also allow a determination of how the differential shift changes with bombardment angle.

If an accurate measurement of the magnitude of the differential shift under normal incidence ion bombardment is required, then a non reactive ion species such as Ar^+ could be used. This also prevents oxide formation. However, the value of the differential shift could be different due to the change in ion species. This could also be investigated by using Cs^+ primary ions.

The differential shift for the capped layers indicates that the initial sputter rate is higher than that for the steady state regime. This is due to the oxygen initially sputtering pure silicon and then later sputtering SiO_2 where some of the primary ion energy has to be spent breaking Si-O bonds. If argon was used to sputter SiO_2, the sputter rate should increase in the steady state regime since the argon would reduce the oxide and the differential shift would be away from the surface.

Finally, it may be that that the differential shift is a function of the depth of the feature being examined. To investigate this a series of different thickness caps should be grown and the differential shifts determined. Again, different thicknesses are to be preferred to different implant energies, since, the sputter rate variation is what is wanted and the ion yield variation would mask this. A table of differential shift versus depth could then be drawn up and used to correct the depth scale after analysis.

Matrix	Implant	Energy /keV	μ_1 /Å	σ /Å	τ	β	k
A - Si	BF_2	4	173.77	8.151E-3	1.09	3.48	-0.46
		6	161.38	7.350E-3	1.25	4.05	-0.65
		8	193.98	8.549E-3	1.55	5.14	-1.01
	P	4	193.59	9.170E-3	1.01	3.28	-0.40
		6	211.15	9.160E-3	1.23	3.71	-0.53
		8	200.26	7.833E-3	1.02	3.05	-0.34
	As	4	176.24	7.820E-3	0.98	3.95	-0.89
		6	199.46	9.707E-3	1.13	3.57	-0.49
		8	240.43	9.830E-3	1.36	3.86	-0.57
Si	BF_2	4	205.98	1.291E-2	1.99	8.05	-3.35
		6	208.03	1.260E-3	1.81	6.79	-1.98
		8	221.42	1.086E-2	1.05	3.31	-0.41
	P	4	244.33	1.323E-2	1.09	3.45	-0.45
		6	266.80	1.393E-2	1.07	3.16	-0.38
		8	265.42	1.160E-2	0.95	2.90	-0.31
	As	4	173.90	7.986E-3	1.26	4.55	-1.01
		6	188.49	8.280E-3	1.45	4.47	-0.75
		8	212.81	8.230E-3	1.30	3.53	-0.49
SiO_2	BF_2	4	144.88	7.815E-3	1.24	4.45	-0.93
		6	196.83	1.202E-2	1.17	4.37	-1.01
		8	217.64	1.473E-2	1.23	4.55	-1.07
	P	4	153.14	8.670E-3	1.14	4.81	-4.11
		6	213.74	1.174E-2	0.86	3.34	-0.43
		8	221.03	1.065E-2	1.16	3.68	-0.52
	As	4	155.72	7.050E-3	1.25	7.24	+0.45
		6	218.52	1.036E-2	0.90	3.79	-0.86
		8	295.41	1.416E-2	1.43	4.58	-0.89

TABLE 4.1

Complete set of projected range R_p, standard deviation σ, skewness τ and kurtosis β. The value of the criterion k, described in the text, is also shown.

CHAPTER 5

INVESTIGATION OF SPUTTER RATE CHANGES

5.1 Introduction

In semiconductors, ion implantation is used to produce shallow junctions in the material. When a crystalline material undergoes ion implantation the lattice structure is damaged and there is a localised area of high point-defect density in the vicinity of the implant maximum. Under heavy-ion bombardment e.g.arsenic, the crystal is amorphised (Prussin et.al. 1985). After implantation, an annealing stage is needed to incorporate the dopant onto active lattice sites and also to recrystallize the lattice. However, simple annealing may cause the point defects to precipitate to form larger defects, such as stacking faults and dislocation loops (Hasko et.al 1985), (Dowsett et.al 1987).

In SIMS, ion implanted standards are used to calibrate the concentration scale of depth profiles and these standards are as implanted, no annealing has taken place and hence, the damage associated with the implantation is still present.

In the vicinity of the damaged layer there would be a localized difference of density and hence the sputter rate would be expected to change. It was decided to investigate whether the presence of a polycrystalline or amorphous damaged layer altered the sputter rate of

silicon during a depth profile. If the sputter rate did change then the calibration of any depth profile would be made very difficult. For example, the amount of damage induced is dose dependant, if the sputter rate change depended on the amount of damage then to deconvolute the effect of the damage on the sputter rate the concentration of dopant would have to be known, but to calibrate the concentration scale the depth scale also needs to be calibrated.

5.2 Experimental

To discover whether the sputter rate varied with depth in high dose unannealed implants, a series of experiments were carried out. The samples used were 10^{16} atoms cm^{-2} 20keV BF_2 implanted into silicon and capped with a 50nm Si-MBE grown capping layer (see chapter 4) and five 25keV boron implants into silicon at doses of 10^{16}, 10^{15}, 10^{14}, 10^{13} and 10^{12} atoms cm^{-2} in order to see if any changes detected were dose and hence damage, dependant.

The depth profiles were carried out for different lengths of time. The implanted species was monitored so that the experiment could be terminated at the correct point on the profile.

The first profile of a series was taken well past the implant and into the background, so that the count rates and sputter times could be compared with later runs

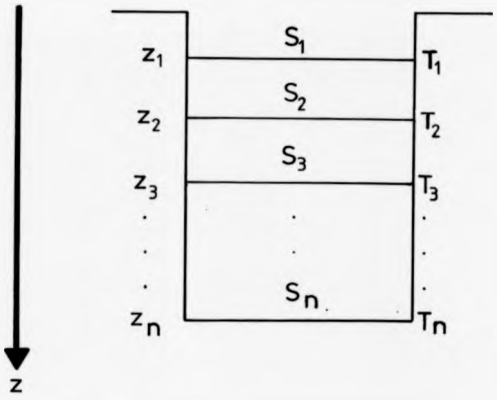

$$S_n = \frac{z_n - z_{n-1}}{T_n - T_{n-1}}$$

FIGURE 5.1. Schematic showing the method for calculating the differential sputter rate.

to ensure that any variation in the primary beam parameters could be detacted.

All the experiments were carried out on EVA 2000 using 4keV O_2^+ ions at normal incidence into a 400 x 400µm crater with a 1mm x 1mm preclean for 100 seconds. The depths of the craters were measured after each analysis on a Sloan Corporation Dektak 3030 Auto II.

The analysis conditions were checked after each experiment to ensure that they were the same for each sample. This enabled a differential sputter rate calculation to be made for each sample, figure 5.1.

Each sample n, was etched to a depth z_n in a time T_n. The sputter rate for each sample was z_n / T_n. The differential sputter rate was calculated as $z_n - z_{n-1}$ / $T_n - T_{n-1}$.

5.3 Results

The results obtained from the capped BF_2 layer is shown in figure 5.2. There was a variation of a factor of 2.5 in the sputter rate with the minimum sputter rate occuring just after the peak.

The results for the boron implants are given in table 5.1 showing sputter time, depth, incremental depth and differential sputter rate in angstroms/second. The results are plotted in figure 5.3. There was a variation of 250% in each case but the positions of the maximum and minimum sputter rate were different for each dose and

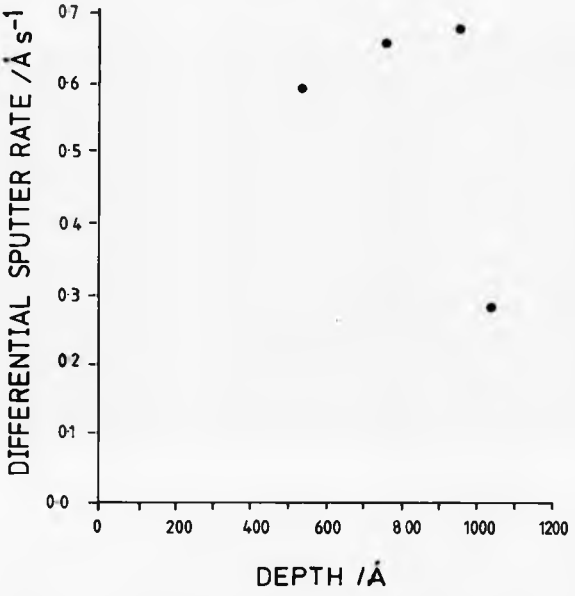

FIGURE 5.2. Differential sputter rate measurement for a 10^{15}, 20 keV BF_2 implant in a capped sample (see chapter 4). Maximum variation is 250Å.

even the lowest dose implant exhibited a sputter rate change.

All the craters were measured in the x-scan direction on the Daktak. A typical trace is shown in figure 5.4. The gated area of 125μm in the centre of the crater is also indicated. The maximum unevenness in the gated area was 2%.

5.4 Discussion

An inaccuracy of ±1% in the depth scale affects the sputter rate measurement by a much larger amount. Table 5.2 gives the measured depth and the calculated depths of a 2% error. It also shows the maximum and minimum sputter rates for these depths. These sputter rates were obtained by subtracting z_{1max} from z_{2min} for the minimum sputter rate and z_{1min} from z_{2max} for the maximum sputter rate. These were then taken as error bars for figure 5.3 and the replotted data and errors is shown in figure 5.5. There is still a variation in the sputter rate but it is now less than 10%.

To check that the 2% error in depth was reproducible the depths of the craters were remeasured in the y-scan direction. The depth scan obtained is shown in figure 5.6. There was a linear unevenness of 10% within the gated area. If the data is replotted with ±5% error bars the result is as shown in figure 5.7. From this graph an

FIGURE 5.3. Differential sputter rate measurement for five different boron doses implanted into silicon.

assumption of constant sputter rate over the depth profile is not shown to be invalid.

Any uneveness in the bottom of a SIMS crater is due to an inhomogeneous ion beam dose across the crater. This is due to either non-linearity in the rastering electronics, inhomogeneity in the scan plate electric field or to improper alignment of the primary beam or any combination of these. The fact that the x-scan was almost uniform indicated that the beam was properly aligned in the y-plane.

The amount of uneveness present in the craters meant that any measurement of the differential sputter rate due to implantation damage could not be made.

In practice, a large uneveness like that found in this study, will lead to errors in calibrating the depth scale of depth profiles.

To test the accuracy of depth measurements the same crater was given to different operators to measure. They obtained a reproducibility of 1% or better if the scan was done in the y-direction. If the scan was taken in the x-direction the reproducibility was down to 10% depending on which part of the sloping crater bottom the readings were taken. This reproducibility error of 10% is in spite of the fact that individual traces in the x-direction were flat to 1-2%.

It has been shown (McPhail et. al. 1988c) that uneven crater bottoms can distort the shape of many

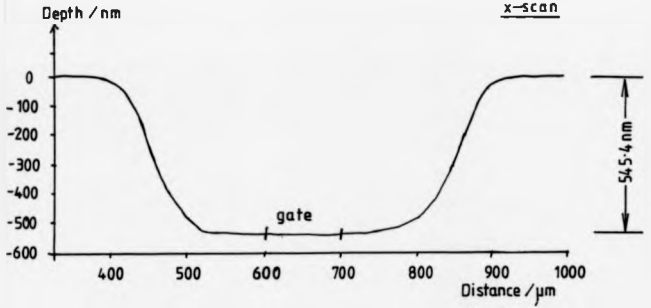

FIGURE 5.4. Dektak trace of profile crater measured in the x direction. The unevenness in the gated area is 2%.

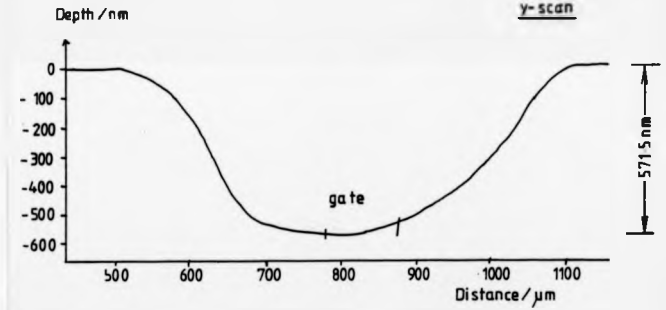

FIGURE 5.6. Dektak trace of profile crater measured in the y direction. The unevenness in the gated area is 10%.

features profiled by SIMS. This is due to nonuniform breakthrough of the crater into buried features leading to an artificial broadening of interfaces. Multilayer structures with rapid doping transitions are the worst affected, although implants show only a marginal effect. A 10% uneveness in a crater leads to only a 3% inaccuracy in the depth calibration for an implant.

5.5 Conclusion

This study attempted to show that there was a change in sputter rate induced by a change in density due to implantation damage in the region of the projected range of an unnanealed implant. It has not been possible to confirm or deny that such an effect is present due to the effect of macrotopography in the crater bottom.

If an ion scanning system that produces flat bottomed craters is developed then the experiment can be repeated and the effect of density changes due to ion implantation damage can be measured.

The difference in sputter rate between crystalline and amorphous silicon is only 10%. To detect this using the method described here requires that the craters produced should be flat and parallel with the starting surface to less than one per cent. One method of doing this is to increase the analysed area to minimize the ion beam variation within the gated area.

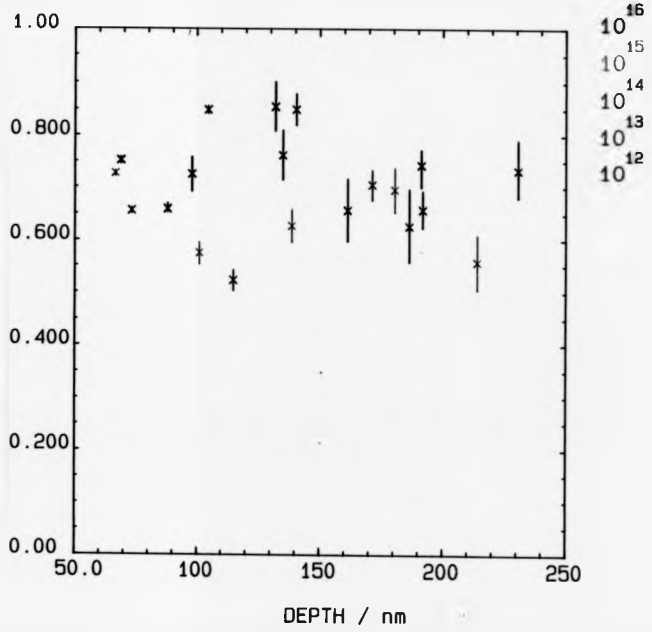

FIGURE 5.5. Error bars for differential sputter rate measurement shown in figure 5.3 assuming 2% unevenness.

Ideally, the most reliable method however is to ensure that the ion density across the scanned area is uniform and this automatically produces flat bottomed craters.

In order to compensate for any sputter rate variation an in-situ depth calibration technique should be used which would allow each data point to be associated with the correct depth. This would ensure that variations in sputter rate were automatically accounted for. One such method is to use a laser optical technique (Kempf 1982). This method however is not very useful in the analysis of semiconductors since the optical constant of silicon changes depending on the dopant and doping concentration as well as any interfaces in the material. In order to use this method reliably, it would be necessary to know the concentration of the species that was being measured.

The importance of flat crater bottoms in the gated area of SIMS depth profiles cannot be overstated. Until they are flat, significant problems will occur in the analysis of many of the new structures being produced by the semiconductor industry today such as heterostructures and strained layer superlattices grown by MBE.

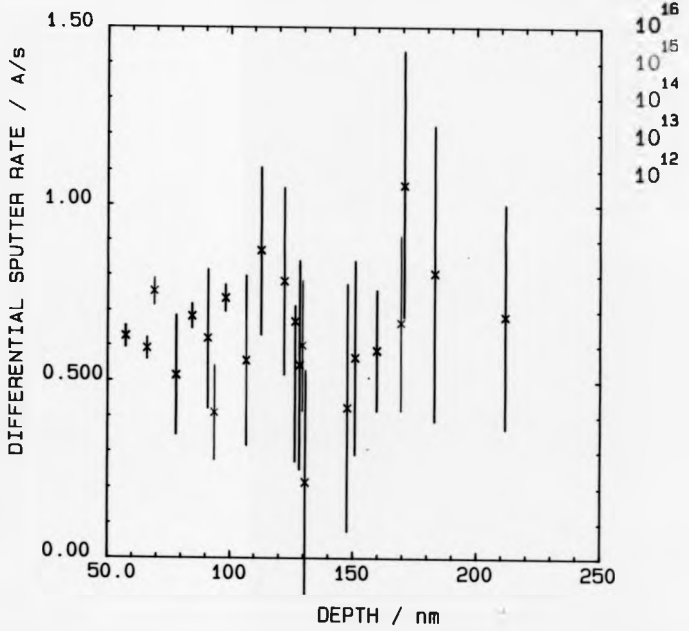

FIGURE 5.7. Differential sputter rate measurement for the five different boron doses based on a depth measurement taken in the y direction and including error bars for ±1% unevenness.

Boron Dose atoms/cm^2	Sputter Time s	Depth Å	Differential Depth Å	Differential Sputter rate Å/s
10^{16}	1000	689	689	0.752
	1400	979	290	0.725
	1800	1321	342	0.855
	2600	1914	593	0.741
	7000	4636	2722	0.619
10^{15}	1000	666	666	0.727
	1600	1011	345	0.575
	2200	1388	377	0.628
	2800	1806	418	0.696
	3400	2141	335	0.558
	9000	5825	3684	0.658
10^{14}	1200	732	732	0.656
	2000	1150	418	0.523
	2800	1714	564	0.705
	7000	4117	2403	0.572
10^{13}	1400	1046	1046	0.849
	1800	1351	305	0.763
	2200	1614	263	0.658
	2600	1865	251	0.628
	3200	2307	442	0.734
	8380	5808	3501	0.675
10^{12}	1500	878	878	0.659
	2120	1405	527	0.850
	2900	1919	514	0.699
	5400	3714	1795	0.718

TABLE 5.1

Sputter rate data for each boron implant. For differential sputter rate determination, see text.

Boron Dose atoms/cm²	Depth Å	Max. Depth Å	Min. Depth Å	Max. S.rate Å/s	Min. S.rate Å/s
10^{16}	689	694.5	683.4	0.758	0.746
	979	986.8	971.1	0.758	0.691
	1321	1331.5	1310.4	0.901	0.809
	1914	1929.3	1898.6	0.773	0.701
	4636	4673.0	4598.9	0.630	0.606
10^{15}	666	671.3	660.6	0.733	0.721
	1011	1019.0	1002.9	0.597	0.553
	1388	1399.1	1376.8	0.660	0.596
	1806	1820.4	1791.5	0.739	0.654
	2141	2158.1	2123.8	0.611	0.506
	5825	5871.6	5778.4	0.669	0.464
10^{14}	732	737.8	726.1	0.661	0.651
	1150	1159.2	1140.8	0.541	0.503
	1714	1727.7	1700.2	0.773	0.676
	4117	4149.9	4084.0	0.583	0.561
10^{13}	1046	1054.3	1037.6	0.856	0.842
	1351	1361.8	1340.1	0.811	0.715
	1614	1626.9	1601.0	0.717	0.598
	1865	1879.9	1850.0	0.697	0.558
	2307	2325.4	2288.5	0.792	0.681
	5808	5854.4	5761.5	0.688	0.663
10^{12}	878	885.0	870.9	0.669	0.654
	1405	1416.2	1393.7	0.879	0.821
	1919	1934.3	1903.6	0.693	0.625
	3714	3743.7	3684.2	0.736	0.697

TABLE 5.2

Table of the measured depth and the maximum and minimum depths calculated for a 2% error in the depth measurement. These give the maimum and minimum differential sputter rates shown in the two columns on the right.

CHAPTER 6

RASTER SCANNER

6.0 Overview

It has been assumed for several years that the depth resolution of a SIMS experiment varies linearly with depth (Werner et.al. 1974). The reason for this is uneven etching causing profile broadening (McPhail et.al. 1986a).

It was seen in the previous chapter that a flat crater bottom is crucial to the outcome of SIMS experiments, especially since the advent of quantum well heterostructures and similar devices in the semiconductor industry.

In this chapter, two raster scanners are discussed. One is a new computer controlled raster scanner for use with a new SIMS instrument - EVA 3000. The other is a slightly simpler raster scanner for use with EVA 2000 with fewer programmable features. The effect of different raster scan plate geometries will also be discussed.

6.1 Introduction

A raster scanner for use in SIMS provides a digitally generated scan waveform at two different frequencies. The fast scan is in the x-direction and generates the line signal and the slow scan is in the y-

direction which generates the frame signal. The scan waveform produced is a staircase wave and the sharp edge is the flyback signal.

6.2 Computer Contolled Raster Scanner

The aim of this project was to produce a raster scanner that would have all the operational parameters such as frame size, frame time, gate size and gate position under computer control. The block diagram of the raster scanner is shown in figure 6.1

The frame time was specified to be variable from 0.005 seconds to 3000 seconds. This range was to enable different analysis procedures to be carried out. The fastest frame times are for real time imaging where data is acquired for ≈0.1μs per pixel. These frame times are also used for secondary electron and total ion imaging of samples where the rapid dwell time limits the damage to the sample. Long frame times are used for line scan acquisition of data where long dwell times are needed to produce a reasonable count rate.

The electronic gate (chapter 2) was programmable so that the size and position of the gate could be independently set for both the x and y directions, so as to avoid particulates on the sample surface. A reset line was included so that the computer did not have to wait for the end of frame pulse before starting an

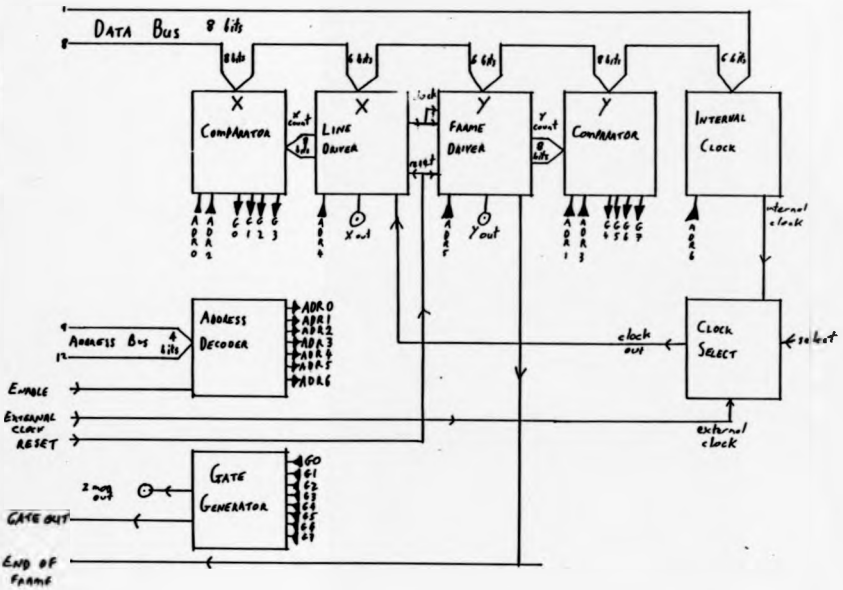

FIGURE 6.1. Block diagram of the computer controlled raster scanner described in the text.

experiment, since, in the case of the very long frame times, this was not feasible.

6.2.1 Implementation

The clock was generated from a 13.1072MHz quartz crystal and by using a combination of divide by 10, 12 and 16 integrated circuits, divided down so as to give computer selection of times on a .5, 1, 1.5, 2 and 3 scale over almost 6 decades of time.

The clock pulses go to the x (line) driver board where they are divided by 256 by two four bit counters to give an 8 bit parallel count, this is used to derive the gating signals. When the count reaches 255 a pulse is output to the y (frame) board thus giving the correct 256 to 1 ratio of the line and frame timings. The 8 bit count goes to the most significant bits of a 14 bit D/A converter (Analog Devices 7475KN). This generates a -10 to +10V sawtooth waveform which goes to an oscilloscope and also to the multilplying input of another D/A converter. The frame size is sent from the computer to the DAC as a 6 bit number. The DAC then outputs a sawtooth waveform which is n/32 times the + and -10V waveform that was input. This output goes to two high voltage amplifiers which have a fixed gain of ten times, and drives the scan plates. The gate pulses are formed by comparing the running count with the 8 bit values entered from the computer at the start of the

experiment. TTL logic is used to output a positive signal whenever the beam is within the gated area. At the end of the frame a positive pulse is output to the computer so that it can change any of the depth profiling parameters while the beam is outside the gate.

If a non uniform frame crater is required, e.g. for producing a bevelled crater (McPhail et.al. 1988a) then the external clock input line can be used to take a signal from the computer or other external source to step the beam.

Preliminary results on the linearity of the raster scanner conducted on EVA 2000 have given good results. However it was not possible to connect it to the RML380Z microcomputer that controls the instrument and a BBC B micro was used instead. This meant that the system could not acquire a depth profile, just drill a crater.

The ultimate test of this raster scanner will have to wait until it is used on EVA 3000 in conjunction with its control interface.

6.3 Modification to EVA 2000 Raster Scanner

The raster scanner supplied by Atomika GMBH was discovered to be of insufficient accuracy when periodic doping structures grown by the Warwick MBE group (McPhail et.al. 1988b) were first profiled. This showed that there was an inhomogeneity in the ion dose across the crater on EVA 2000. This was initially traced to non-linearities

FIGURE 6.2. Graph of output response of a DAC80 digital to analogue converter, showing the output in mV for each input value.

in the digital-to-analogue converters used in the scan unit.

Although the DACs were performing within their specifications, they were not accurate enough to give a constant scan rate and hence a constant ion dose across the sample, therefore, the craters were not flat.

It was decided to replace the 8 bit DACs with 14 bit DAC80s which had the bottom 6 bits tied to earth potential. In this configuration the linearity of the device goes from one half the least significant bit to 1/128 lsb thus producing a better scan.

The output of the DAC80 is shown in figure 6.2, This is a plot of input number versus output voltage. The DAC80 contains an inbuilt amplifier so the output from the device is a voltage instead of a current which eliminates the need for external components.

In the original Atomika unit the high voltage output amplifiers were fixed gain devices with the input being determined by the output of an analogue multiplier. This again introduced non-linearities in the output waveform. The analogue multiplier was exchanged for a discrete component DAC driven from the computer and the output amplifiers were redesigned (Lovejoy 1986).

Measurements on the clock signal of the scan unit revealed that the pulses were non uniform. These were derived from a free running 555 timer. This device is not totally stable and depends on an R-C network to

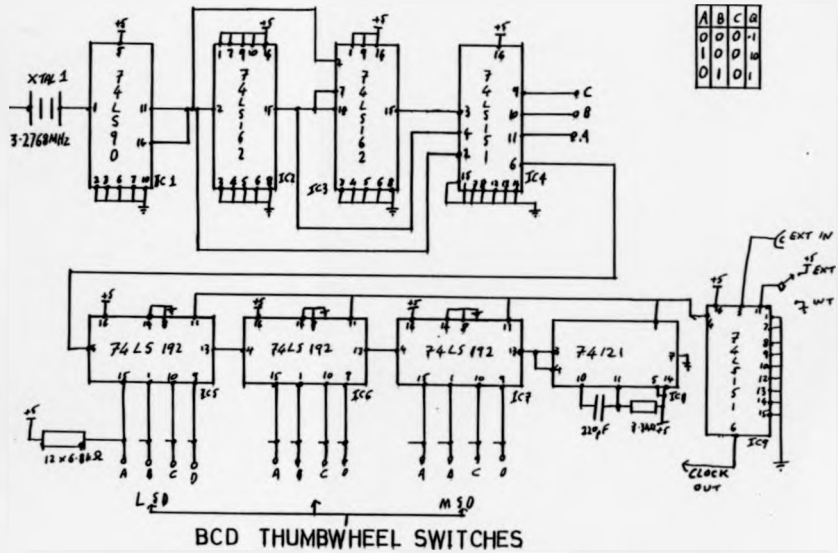

FIGURE 6.3. Circuit diagram of the new clock generator for EVA 2000's raster scanner.

produce its reference. This enabled the unit to drift unpredictably with time.

The 555 timer was replaced with a quartz crystal oscillator and the clock circuitry was replaced to give a larger range of frame times. The circuit diagram of the new clock circut is shown in figure 6.3.

The clock pulses go through three divide by 10 counters giving three basic frame time multipliers: x0.1 , x1 and x10. This frame time multiplier can be selected from the front panel by a switch and the actual frame time set by BCD thumbwheel switches. The frame time is generated by three consecutive divide-by-n counters, where n is set by the thumbwheel switches. This circuit enables the operator to choose a frame time varying from 0.1 to 9990 seconds.

An 74LS151 demultiplexer is used to select whether the internal or an external clock is to be used to drive the raster unit. An external y-input line is also supplied so that bevels and other non uniform crater shapes can be produced.

All these changes combined produced a raster scanner with ≈1% linearity across the cratered area. Lately, the quadrupole scan plates, which have always been suspect, have been replaced with a discrete scan unit (Dowsett 1989) and this in conjunction with the heavily modified Atomika unit have produced craters that are very flat indeed <0.1% (Cooke 1989).

6.4 Conclusion

In order to generate a flat bottomed crater parallel to the sample surface it is necessary to ensure that there is a uniform primary ion dose across the crater. This requires a uniform scan waveform as well as a uniform deflection field in the ion column.

Two different methods of generating a uniform scan were described here. One was completely new and totally computer controlled and the other was a modification of an existing, commercially available unit.

Coupled with a discrete scan system, this second unit will now produce flat bottomed craters for use in SIMS depth profiles which will not contribute any further broadening in the analysis of thin layer structures besides that already produced by fundamental effects.

The changes described here are only for those SIMS instruments that use normal ion incidence when depth profiling. For experiments that require non-normal incidence or in instruments that have non-normal incidence as a design feature, these changes alone will not produce flat bottomed craters parallel to the surface. In order to achieve this a method of changing the pixel dwell times will have to be found.

CHAPTER 7

CONCLUSIONS

In this thesis a method of quantifying implant profiles by taking the first four moments has been proposed. This allows information about implants to be transmitted meaningfully between laboratories. This technique has been applied to the determination of the differential shift for crystalline and amorphous silicon.

Using moments enabled the effect of the pre-equilibrium region on the leading edge of shallow implants to be identified. Capping layers grown by Si-MBE have been successfully used to overcome this problem and give a determination of the differential shift. This has been determined only using amorphous caps. From the data presented here, it seems that in the initial, near surface region the shift is inwards and only deeper into the material is it outwards. Measuring the differential shift in capping layers of many different thicknesses would allow a function to be constructed that could correct for the differential shift throughout the profile.

At present only amorphous layers have been grown which leads to the contamination of the interface due to trapped impurities. Future investigations could use crystalline MBE layers that have been heat treated before growth to remove the buried impurities, but the effect of

the heat treatment on the samples would have to be investigated first to ensure that no diffusion took place. Epitaxially grown capping layers would allow the differential shift to be accurately measured in crystalline silicon.

At present it is only possible to grow a capping layer on a complete three inch wafer. A useful future development would be to allow this technique to be used on smaller pieces like those used for SIMS experiments.

The use of three different dopant species in the determination of the differential shift allowed the presence of arsenic segregation in front of an advancing oxide interface to be inferred.

The behaviour of the differential shift in different matrices led to an investigation into how the sputter rate changed in heavily damaged regions of a crystalline material caused by ion implantation. This variation, if any, would lead to great difficulties in the post analysis calibration of both the depth and concentration scales of a depth profile.

The investigation described here revealed gross inhomogeneities in the ion beam dose across the scanned area. This made determination of the differential sputter rate impossible. However, this result led to an investigation of the raster scan unit of EVA 2000 and lead to it being effectively rebuilt. The quadrupole scan plates themselves were replaced by a discrete plate

deflection system which now produces craters that are flat and parallel to the sample surface to 0.8nm in 1500nm (0.05%).

The differential shift measurements need to be repeated at non normal angles of incidence. This would reduce the segregation effects seen here. It would also enable any variation in the differential shift with angle to be observed. This is important since magnetic sector instruments use non normal incidence and these measurements would enable results to be transferred between instruments.

The procedure should also be carried out using other ion species such as caesium and argon. This would again reduce the segregation effect and also show how the differential shift varies with primary ion. This is important since the differential shift is primarily a pre-equilibrium effect and the processes occuring during this time depend on the species taking part.

Flat bottomed craters parallel to the starting surface are going to be critical in the future with the advent of new materials technology. III-V quantum well heterostructures and Si-Ge strained layer superlattices are just two technologies that are starting to appear and require SIMS analysis. To give reliable information to the growers of these structures it is vital that SIMS analysts are confident that they have minimised the

instrumental causes of profile distortions. Predominant among these is uneven etching.

To produce flat bottomed craters in the future it may be necessary to produce 'intelligent' raster scanners that can change the dwell time per pixel to eliminate any inhomogeneities generated in the scan electronics. The technology to do this is not difficult and is, in fact present in many laser printers.

Another semiconductor industry driven requirement will be the ability to generate two and three dimensional analyses. This is because of the constantly shrinking size of the active regions in integrated circuits. The manufacturers will want to know how the dopants behave in-situ, e.g. how much diffusion has taken place in the lateral direction from drain and source regions.

This requirement will in turn lead to the need for better ion sources which can produce a sub-micron spot for 2-D imaging purposes as well as high current densities for depth profiling.

In general SIMS instrumentation has to be made more reproducible so that operators can set up the primary and secondary columns automatically from existing data files. This requires a much higher degree of ion optical alignment in the basic design of SIMS instruments, as well as a far greater degree of computer control. The aim should be that all instrumental parameters should be controlled by the computer and the electronics should

only have an on/off switch on the front panel. This would enable the technique to be used as easily as an electron microscope is today.

REFERENCES

G.Blackmore, S.Courtney, C.R.Whitehouse, E.A.Clark, D.E.Sykes, R.Collins, (1988), in Proceedings of SIMS VI, edited by A.Benninghoven, A.M.Huber and H.W.Werner, p399, John Wiley, London.

Augustus, P.D., G.D.T.Spiller, P.Knightley, G.R.Thomas, R.Webb, E.A.Clark, (1988), in Proceedings of SIMS VI, edited by A.Benninghoven, A.M.Huber and H.W.Werner, p485, John Wiley, London.

Barlow, R.D., M.G.Dowsett, P.Rosser, (1988), presented at Quantitative Surface Analysis-5, Teddington, London.

Benninghoven, A., R.J.Colton,D.S.Simmons, H.W.Werner eds., (1986), Proceedings of SIMS V, Springer Verlag, Berlin.

Benninghoven, A., A.M.Huber, H.W.Werner eds., Proceedings of SIMS VI, John Wiley, London, (1988).

Boudewijn, P.H., H.W.Akerboom, M.N.C.Kempeners, Spectrochemica Acta, 19B, 1567, (1984).

Clark, E.A., M.G.Dowsett, G.D.T.Spiller, G.R.Thomas, P.D.Augustus, I.Sutherland, (1988), Vacuum, 38, 937.

Clark, E.A., M.G.Dowsett, G.D.T.Spiller, G.R.Thomas, I.Sutherland, (1988), to be published in Surface and Interface Analysis.

Clegg, J.B., (1986), Proceedings of SIMS V, edited by A.Benninghoven, R.J.Colton, D.S.Simmons and H.W.Werner, p112, Springer-Verlag, Berlin.

Collins, R., (1986), Rad. Effects, 98.

Cooke, G.A, (1989), Private Communication.

Deline, V., (1986), Nucl. Inst. and Methods, 218, 316.

Dowsett, M.G. and P.J.Mole, (1982a), Solid State Devices Research Memo No.111, GEC Hirst Research Centre, unpublished.

Dowsett, M.G., (1982b), unpublished.

Dowsett, M.G., E.H.C.Parker, R.M.King, P.J.Mole, (1983a), J. Appl. Phys., 54, 6740.

Dowsett, M.G. and E.H.C.Parker, (1983b), Int. Journ. Mass Spec. and Ion Phys., 52, 299.

Dowsett, M.G., J.W.Heal, H.Fox, E.H.C.Parker, (1986a), in Proceedings of SIMS V, edited by A.Benninghoven, R.J.Colton, D.S.Simmons and H.W.Werner, p176, Springer-Verlag, Berlin.

Dowsett, M.G., R.M.King, H.Fox, E.H.C.Parker, (1986b), in Proceedings of SIMS V, edited by A.Benninghoven, R.J.Colton, D.S.Simmons and H.W.Werner, p179, Springer-Verlag, Berlin.

Dowsett, M.G., D.S.McPhail, E.H.C.Parker, H.Fox, (1986c), Vacuum, 36, 913.

Dowsett, M.G., unpublished, (1987).

Dowsett, M.G., E.A.Clark, M.Lewis, D.J.Godfrey, (1988a), in Proceedings of SIMS VI, edited by

A.Benninghoven, A.M.Huber and H.W.Werner, p725, John Wiley, London.

Dowsett, M.G., (1988b), Private communication.

Dowsett, M.G., (1989), Private Communication.

Elderton, W.P. and W.P.Johnson, (1969), Systems of Frequency curves, Cambridge University Press.

Frantsuzov, A.A. and I.I.Makrushin, (1976), Thin Solid Films, 32, 247.

Godfrey, D.J., R.A.McMahon, D.G.Hasko, H.Ahmed, M.G.Dowsett, (1985), Mat. Res. Soc. Symp. Proc., 36, 143.

Hasko, D.G., R.A.McMahon, H.Ahmed, W.M.Stobbs, D.J.Godfrey, (1985), Inst. Phys. Conf. Ser., No.76 Sec.3, 99.

Hensel, E., K.Wollschläger, D.Schulze, U.Kreissig, W.Skorupa, J.Finster, (1985), Surface and Interface Analysis, 7, 207.

Hofker, W.K., D.P.Oosthoek, N.J.Koeman, H.A.M.De Grefte, (1975), Rad. Effects, 24, 223.

Houghton, R.F., G.Patel, W.Y.Leong, T.E.Whall, E.H.C.Parker, R.A.A.Kubiak, R.Naylor, (1987), J. Crystal Growth, 81, 326.

Huber, A.M. and G.Morillot, (1986), Proceedings of SIMS V, edited by A.Benninghoven, R.J.Colton, D.S.Simmons and H.W.Werner, p353, Springer-Verlag, Berlin.

Kelly, R., (1985), Surface and Interface Analysis, 7, 1.

Kempf, J., (1982), Surface and Interface Analysis, 4, 116.

Kirschner, J., (1985), Nucl. Inst. and Methods, B7/8, 742.

Kubiak, R.A.A, W.Y.Leong, M.G.Dowsett, D.S.McPhail, R.Houghton, E.H.C.Parker, (1986), Journ. Vac. Sci. Technol., A4, 1905.

Leighton, C., (1987), Private Communication.

Liebl, H., (1983), Vacuum, 33, 525.

Lindhard, J.M.Scharff, H.Schiott, (1963), Mat. Fys. Med. Dan. Viol. Selsk., 33, 1.

Littlewood, S.D. and J.A.Kilner, (1988), J. Appl. Phys., 63, 2173.

Lovejoy, A., (1986), Private Communication.

Maul, J.L. and K.Wittmaack, (1975), Surf. Sci., 47, 358.

McPhail, D.S., M.G.Dowsett, E.H.C.Parker, (1986a), Vacuum, 36, 997.

McPhail, D.S., M.G.Dowsett, E.H.C.Parker, (1986b), J. Appl. Phys, 60, 2573.

McPhail, D.S. and M.G.Dowsett, (1988a), in Proceedings of SIMS VI, edited by A.Benninghoven, A.M.Huber and H.W.Werner, p269, John Wiley, London.

McPhail, D.S., E.A.Clark, M.G.Dowsett, H.S.Fox, A.Lovejoy, (1988b), in Proceedings of SIMS VI, edited by A.Benninghoven, A.M.Huber and H.W.Werner, p495, John Wiley, London.

McPhail, D.S., M.G.Dowsett, H.Fox, R.Houghton, W.Y.Leong, E.H.C.Parker, G.Patel, Surface and Interface Analysis, 11, 80, (1988c).

Miethe, K., W.H.Gries, A.Packer, (1986), Proceedings of SIMS V, edited by A.Benninghoven, R.J.Colton, D.S.Simmons and H.W.Werner, p347, Springer-Verlag, Berlin.

Prussin, S., D.I.Margolese, R.N.Tauber, (1985), J. Appl. Phys, 57, 180.

Reuter, W. and K.Wittmaack, (1980), Appl. Surf. Sci., 5, 221.

Rysell, H. and K.Hoffman, (1980), in Ion implantation.

Siedl, T.E., (1983), in VLSI Technology.

Sigmund, P., (1969), Physical Review, 184, 383.

Sigmund, P., (1974), Appl. Phys. Lett., 25, 169.

Slodzian, G., (1983), in Applied Charged Particle Optics A, A.Septier ed., Academic Press.

Slusser, G.J., (1986), in proceedings of SIMS V, edited by A.Benninghoven, R.J.Colton, D.S.Simmons and H.W.Werner, p331, Springer-Verlag, Berlin.

Sze, S.M. ed., (1983), VLSI Technology, McGraw Hill.

Vandervorst, W., H.E.Maes, R.F.De Keersmaecker, (1984), J. Appl. Phys., 56, 1425.

Vandervorst, W., F.R.Shepherd, M.L.Swanson, H.H.Platner, O.M.Westcott, I.V.Mitchell, (1986), Nucl. Inst. and Methods, B15, 201.

Wach, W. and K.Wittmaack, (1981), Nucl. Inst. and Methods, 191, 327.

Werner, H.W., (1974), Vacuum, 24, 493.

Williams, P., (1979), Surf. Sci., 90, 588.

Williams, P., (1980), J.E.Baker, J.A.Davies, J.E.Jackman, Appl. Phys. Lett., 36, 842.

Wittmaack, K., (1974), Nucl. Inst. and Methods, 118, 99.

Wittmaack, K., (1976), Appl. Phys. Lett., 29, 552.

Wittmaack, K., (1977), Appl. Phys., 12, 149.

Wittmaack, K., (1979), J. Appl. Phys., 50, 493.

Wittmaack, K., (1980), Scanning, 3, 133.

Wittmaack, K., (1981), Appl. Surf. Sci., 9, 315.

Wittmaack, K., (1982a), Vacuum, 32, 65.

Wittmaack, K., M.G.Dowsett, J.B.Clegg, (1982b), Int. Journ. Mass Spec. and Ion Phys., 43, 31.

Wittmaack, K., (1984), Vacuum, 34, 119.

Wittmaack, K., (1985), Appl. Phys. A, 38, 235.

Wittmaack, K. and N.Menzel, (1987), Appl. Phys. Lett., 50, 815.

Ziegler, J.F., J.P.Biersack, U.Littmark, (1985), The stopping and range of ions in solids Vol 1., Pergamon Press, London.

TITLE A STUDY OF SHALLOW IMPLANTS IN SILICON BY SECONDARY ION MASS SPECTROMETRY

AUTHOR Harvey Stuart Fox

INSTITUTION and DATE University of Warwick 1989